Title: Dynamics of the IFT Machinery at the Ciliary Tip

Alternative Title 1: Dissociation of Kinesin-2 from IFT Trains Controls the Length of *Chlamydomonas* Flagella

Alexander Chien[1]* and Sheng Min Shih[2]*, Raqual Bower[3], Douglas Tritschler[3], Mary E. Porter[3], Ahmet Yildiz[1,2,4]

[1]Biophysics Graduate Group, [2]Physics Department, and [4]Department of Molecular and Cell Biology, University of California, Berkeley, Berkeley, CA, 94720. [3]Department of Genetics, Cell Biology, and Development, University of Minnesota, Minneapolis, MN 55455

*These authors contributed equally to this work.

Correspondence and requests for materials should be addressed to A.Y. (email: yildiz@berkeley.edu).

Abstract:

Intraflagellar transport (IFT) of multiprotein complexes is essential for the elongation and maintenance of eukaryotic cilia and flagella. Due to the traffic jam of multiple trains at the ciliary tip, how IFT trains are remodeled in these turnaround zones cannot be determined by conventional imaging. We developed one-dimensional Photogate imaging and visualized the full range of movement of single IFT trains and motors in *Chlamydomonas* flagella. Anterograde trains split apart and the complexes mix with each other at the tip. Dynein-2 is carried to the tip by kinesin-2 as inactive cargo on anterograde trains. Unlike dynein-2, kinesin-2 detaches from IFT trains at the tip and diffuses in flagella. As the flagellum grows longer, diffusion delays return of kinesin-2 to the basal body, depleting available kinesin-2 for anterograde transport. Our results suggest that dissociation of kinesin-2 from IFT trains serves as a negative feedback mechanism that facilitates flagellar length control.

Introduction

Cilia (or eukaryotic flagella, terms essentially referring to the same organelle) are hair-like organelles that extend from the plasma membrane of nearly all mammalian cells. The core structural component of a cilium is the axoneme, a ring of nine unipolar doublet microtubules surrounding a central pair of singlet microtubules. Cilia play essential roles in cell motility, generate the movement of fluids over multiciliated surfaces, and sense extracellular signals (Satir et al., 2010). To assemble and maintain functional cilia, the IFT machinery (Kozminski et al., 1993) transports axonemal precursors and sensory proteins bidirectionally between the cell body and the ciliary tip. Defects in IFT are linked to a wide range of human diseases including Bardet-Biedl syndrome, retinal degeneration, and polycystic kidney disease (Brown and Witman, 2014).

Intraflagellar cargoes interact with multiprotein complexes known as IFT particles that are organized into larger IFT trains as they enter the flagellum (Cole et al., 1998; Lechtreck et al., 2017; Pigino et al., 2009). In most species, the IFT trains are transported anterogradely from the base to the tip of a flagellum by heterotrimeric kinesin-2 (Kozminski et al., 1995), but some species also use a second homodimeric kinesin that cooperates with the heterotrimeric kinesin-2 to build more specialized sensory cilia (Snow et al., 2004). Once the trains reach the tip, they are reorganized and transported retrogradely to the ciliary base by dynein-2 (Pazour et al., 1999; Porter et al., 1999; Signor et al., 1999). Along the length of a cilium, the activities of kinesin and dynein motors are reciprocally coordinated, such that only one type of a motor is active at a time (Shih et al., 2013). As a result, trains move between the tip and base of the cilium without significant pauses or back-and-forth motion (Dentler, 2005; Engel et al., 2009) and switch directions at the turnaround zones (Ishikawa and Marshall, 2011; Laib et al., 2009; Shih et al., 2013). Dynein-2 requires kinesin-2 activity to reach the ciliary tip, suggesting that it travels as an

inactive passenger on anterograde trains (Iomini et al., 2001; Pedersen et al., 2006; Rompolas et al., 2007). Because anterograde and retrograde IFT trains have different sizes and depart at different frequencies (Dentler, 2005; Iomini et al., 2001), IFT trains must be remodeled at the distal tip and the flagellar base.

The mechanism underlying the remodeling of IFT complexes at the ciliary tip and base cannot be directly observed by conventional microscopy methods because multiple trains coexist in these turnaround zones (Buisson et al., 2013; Iomini et al., 2001; Wren et al., 2013). In this work, we used PhotoGate (Belyy et al., 2017) to limit the number of fluorescent IFT trains entering the flagellum of the unicellular algae *Chlamydomonas reinhardtii*. Using this approach, we monitored the turnaround behavior and remodeling of single IFT trains at the flagellar tip. We also elucidated the mechanisms by which the kinesin and dynein motors are recycled in this process and IFT trains reverse their direction of motion. Dynamics of the IFT tip turnover suggest a new mechanism for how *Chlamydomonas* controls the length of its flagella.

Results

IFT trains split apart and mix with each other at the flagellar tip

To monitor IFT movement, we tracked IFT27, a core component of the IFT complex B, in a *pf18 IFT27-GFP* strain (Engel et al., 2009; Qin et al., 2007). This strain has paralyzed flagella *(pf)* that readily adhere to the glass surface, enabling us to monitor IFT under total internal reflection (TIR) illumination (Engel et al., 2009). Consistent with previous studies (Dentler, 2005; Engel et al., 2009; Iomini et al., 2001; Kozminski et al., 1993; Shih et al., 2013), IFT trains moved processively along the length of flagella, reversing direction at the flagellar tip and base (Figure 1a, Video 1). Cargo reversals along the flagellum were not observed. The velocity of IFT27-GFP was 2.1 ± 0.4 μm s^{-1} in the anterograde direction and 3.0 ± 0.7 μm s^{-1} in the retrograde direction

(Figure 1-figure supplement 1, mean ± s.d., N = 80 trains in each direction). Because a large number of GFP-labeled trains accumulated at the tip, the dwell and departure of individual trains at the tip could not be resolved by conventional TIR imaging (Figure 1a).

To monitor the turnaround behavior of individual IFT trains at the flagellar tip, we developed one-dimensional PhotoGate microscopy (Belyy et al., 2017) to track single fluorescent complexes at the flagellar tip. In this assay, fluorescent trains located at distal parts of a flagellum were initially photobleached by moving a focused laser beam from the tip of the flagellum to near its base. We next opened the "gate" by turning off the focused beam until a single fluorescent train entered the flagellum. The gate beam was repeatedly turned on for 0.2 s at 1 Hz to photobleach any additional anterograde trains entering the flagellum (Figure 1b, Video 2). Under these conditions, less than 1% of anterograde IFT trains were able to pass the gate unbleached. This approach revealed the full range of movement of single fluorescent IFT trains within the flagellum. IFT movement can be divided into three stages: anterograde movement toward the tip, pausing at the tip, and returning to the base by retrograde transport. Pausing and reversal of anterograde trains before reaching the tip were very rare. We directly observed that a single anterograde train splits into multiple retrograde trains at the tip (Figure 1c-e, Figure 1-figure supplement 2a), consistent with the studies of IFT in *Chlamydomonas* (Dentler, 2005) and *Trypanosoma* (Buisson et al., 2013). On average, 2.4 retrograde trains were detected departing from the tip after the arrival of a single fluorescent anterograde train (Figure 1f, N = 97), significantly higher than the measured ratios of retrograde to anterograde train frequencies (~1.6) (Buisson et al., 2013; Dentler, 2005; Iomini et al., 2001; Mijalkovic et al., 2017).

These observations suggested that IFT complexes from different anterograde trains recombine with each other to form retrograde trains at the tip. To test this possibility, we closed the gate

after two or three fluorescent anterograde trains entered the flagellum (Figure 1d,e, Videos 3 and 4) and measured the number and return frequency of retrograde trains departing from the tip. If individual trains split and return without mixing with each other, the number and frequency of fluorescent retrograde trains would be proportional to the number of fluorescent anterograde trains. In contrast, we observed 2.4, 3.6 and 4.2 returning trains on average for one, two, and three incoming trains, respectively (N = 97, 60, 42, Figure 1f). The return frequencies for one, two, and three incoming fluorescent trains were 0.57, 0.71 and 0.76 s^{-1}, respectively. Because the increase was sub-proportional with the number of anterograde trains, we concluded that the fluorescent complexes in the anterograde trains disassemble and mix with a pool of "dark" complexes from the other photobleached trains at the tip before they reorganize into retrograde trains (Figure 1f). Our conclusions are not markedly affected by the limited number of IFT27-GFPs per train (~6) or GFP photobleaching under TIR illumination (0.05 s^{-1}, see Materials and Methods). Monte Carlo simulations revealed that the number of retrograde trains still increases sub-proportionally after photobleaching correction (Figure 1g, Figure 1-figure supplement 3), supporting the mixing of the IFT complexes at the tip before they reorganize into retrograde trains.

IFT tip turnaround is regulated by dynein activity and extracellular Ca^{2+}

When only a single fluorescent anterograde IFT27-GFP train was left unbleached near the base of the flagellum, the average duration between its arrival at the tip and the initiation of the first retrograde train was 3.1 ± 0.3 s (mean ± s.e.m., N = 97, Figure 2a), comparable to the tip resting time of IFT cargos (Craft et al., 2015; Reck et al., 2016; Wren et al., 2013). The tip resting time histogram fits well to a Gamma distribution with a shape parameter of 3 and a rate constant of ~1 s^{-1}, indicating that remodeling of IFT trains occurs rapidly through a multistep process (Figure

2a). After the anterograde trains arrive at the tip, they dwell at the tip through a rate limiting process (τ = 1.3 s, y intercept of Figure 2b) before they can depart from the tip. Because this period (tip remodeling time) is independent of the number of fluorescent anterograde trains (Figure 2b), it may correspond to processing and breakdown of anterograde trains at the tip. The dwell time between the departure of successive fluorescent retrograde trains from the tip increased linearly by 1.7 s on average (tip departure time), suggesting that the tip departure is a purely stochastic process (Figure 2b). When two or three fluorescent anterograde trains were allowed to pass through the gate, the average tip departure times between successive retrograde trains were shorter (1.4 and 1.3 s, respectively). This may be due to an increase in the likelihood of retrograde trains that depart from the tip to have at least one fluorescent GFP.

We also tested various signaling regulators to determine their effect on the tip resting time of IFT27. When extracellular calcium in media (0.34 mM) was chelated using EGTA, the tip departure time of IFT trains increased to 2.8 s (Welch's t-test, p = 0.01), whereas tip remodeling time (1.4 s) remained unaltered (Figure 2c-d). The dynein inhibitor ciliobrevin D increased the tip resting time of IFT27 by over two-fold ($p = 1.3 \times 10^{-4}$). Remarkably, the kinase activator IBMX did not significantly change tip resting time while the kinase inhibitor, H-8, increases the tip resting time by 37% ($p = 1.9 \times 10^{-5}$, Figure 2e and Figure 2-figure supplement 1). The results indicate that calcium has minimal effect on the breakdown of anterograde trains, but may have a regulatory role in the assembly or departure of retrograde trains. Tip turnaround is also sensitive to dynein activity and phosphorylation of the IFT machinery (Liang et al., 2014) or other unidentified substrates.

Kinesin-2 dissociates from IFT trains at the tip

We next turned our attention to the movement of the IFT motors and their exchange at the

flagellar tip. Dynein-2 was tagged with GFP at its light intermediate chain (D1bLIC), which assembles into the dynein-2 complex and rescues *d1blic* mutant phenotypes (Reck et al., 2016). In the *d1blic::D1bLIC-GFP* strain, D1bLIC moved continuously in the anterograde and retrograde directions at velocities similar to that of the IFT trains (Reck et al., 2016) (Figure 3a, Figure 1-figure supplement 1). Kinesin-2 was tagged with GFP at its nonmotor subunit KAP that localizes kinesin-2 to the flagellar base (Mueller et al., 2005). In the *fla3::KAP-GFP* strain, KAP moved primarily in the anterograde direction to the flagellar tip at a similar speed to anterograde IFT27 (Figure 3b, Figure 1-figure supplement 1). Unlike D1bLIC, retrograde traces of KAP were not frequently observed (Engel et al., 2009), suggesting that kinesin-2 dissociates from IFT trains at the tip (Engel et al., 2009, 2012).

We performed PhotoGate assays to directly observe the turnaround behavior of the IFT motors at the flagellar tip. D1bLIC-GFP displayed tip return dynamics comparable to IFT27-GFP (Figure 3c, figure 1-figure supplement 2b, Video 5). After arrival of a single anterograde D1bLIC-GFP train at the tip, we detected on average 2.5 retrograde D1bLIC trains. The average time until the departure of the first retrograde train was 1.8 ± 0.2 s (mean ± s.e.m., N = 60, Figure 3d), with ~1.3 ± 0.2 s between subsequent trains (Figure 3e). PhotoGate imaging of KAP-GFP cells showed that single KAP-GFP trains moved anterogradely to the tip and rested at the tip for 2.2 ± 0.2 s (N = 95). Unlike D1bLIC, individual KAP-GFP particles moved away from the tip by rapid saltatory motion (Figure 3f,g, Figure 1-figure supplement 2c, Video 6). Mean square displacement (MSD) analysis showed that KAP undergoes one-dimensional diffusion at 1.68 ± 0.04 $\mu m^2\ s^{-1}$ (mean ± s.e.m., N = 27 traces) within the flagellum after it departs from the tip (Figure 3h), consistent with the values measured for other proteins such as tubulin and EB1 that undergo diffusion within the ciliary space(Craft et al., 2015; Harris et al., 2016). The splitting of

single KAP-GFP anterograde trains into smaller diffusing particles was not frequently observed (Figure 3-figure supplement 1), presumably because they simultaneously depart from the tip. Similar to IFT27, the tip return time of KAP increased ~50% when the cells were treated with ciliobrevin D ($p = 1.6 \times 10^{-3}$) and H-8 ($p = 2.3 \times 10^{-3}$). Unlike IFT27, EGTA and IBMX had no significant effect on tip return time of KAP (Figure 3-figure supplement 1), suggesting that the tip departures of kinesin and retrograde IFT are independent from each other.

We next investigated whether KAP diffuses along the microtubule track in a linear fashion, similar to a non-processive, microtubule-depolymerizing kinesin, MCAK (Helenius et al., 2006). In this case, KAP clusters would be expected to move along a microtubule, so the fluctuation in KAP position at the perpendicular axis would be similar to the error of single particle tracking. The KAP-GFP particles had lateral fluctuations of 19 ± 2 nm (mean ± s.d.) when moving in the anterograde direction. After departing from the tip, lateral fluctuations of diffusing spots increased to 65 ± 7 nm (Figure 3i,j), comparable to the radius of the axoneme. The intensity of fluorescent spots stayed relatively constant during anterograde transport and diffusion, suggesting that the measured lateral fluctuations are due to diffusive motion rather than decreased tracking precision. We concluded that after KAP detaches from the flagellar tip, it freely explores the space between the flagellar membrane and the axonemal surface rather than sliding along microtubules.

Kinesin-2 carries dynein-2 as an inactive passenger during anterograde IFT

To investigate how kinesin-2 and dynein-2 motors interact with anterograde and retrograde trains and how they are recycled back to the basal body, we transformed a *d1blic* mutant with both *D1bLIC-crCherry* and *KAP-GFP* constructs and simultaneously tracked the movement of KAP and D1bLIC subunits in the rescued cells (Figure 4-figure supplement 1, Video 7). The *D1bLIC-*

188 *crCherry* transgene rescued the flagellar assembly defects previously observed in the *d1blic*
189 mutant, increasing the average flagellar length to 12.2 ± 1.6 µm (mean ± s.d., N = 100 flagella).
190 Both tagged motors were expressed at near wild-type levels (Figure 4-figure supplement 1). The
191 velocities of anterograde and retrograde D1bLIC-crCherry trains were similar to those observed
192 with IFT27-GFP and D1bLIC-GFP labeled trains (Figure 4a, Figure 1-figure supplement 1). In
193 addition, we observed strong co-localization of D1bLIC-crCherry and KAP-GFP on anterograde
194 trajectories (Figure 4a), demonstrating that dynein-2 is carried to the flagella tip by kinesin-2.
195 Only D1bLIC-crCherry trains showed robust retrograde transport, while retrograde traces of
196 KAP-GFP were rarely observed.

197 To determine which motor first departs from the tip after the arrival of an anterograde train, we
198 performed two-color Photogate experiments, allowing us to simultaneously track KAP-GFP and
199 D1bLIC-crCherry from individual anterograde trains (Figure 4b,c). Out of 16 cells that were
200 analyzed, KAP-GFP began diffusive motion before the retrograde movement of D1bLIC-
201 crCherry in 8 cells, D1bLIC-crCherry left the tip before KAP-GFP in 5 cells, and both KAP-GFP
202 and D1bLIC-crCherry appeared to exit the tip simultaneously (within 0.24 s) in 3 cells. These
203 results suggest that kinesin-2 and dynein-2 exit the flagellar tip compartment independently from
204 each other.

205 Using PhotoGate, we have visualized the turnaround behavior of individual components of the
206 IFT machinery at the flagellar tip. We have shown that when IFT trains arrive at the tip, they
207 dissociate from the microtubules into the flagellar matrix. The complexes split apart and mix
208 with complexes from other trains at the flagellar tip before rebinding to the microtubules and
209 initiating retrograde transport (Figure 4d). This dynamic disassembly and reassembly process
210 may lead to differences in the shape and size of anterograde and retrograde trains, as previously

observed (Dentler, 2005; Stepanek and Pigino, 2016). Remarkably, remodeling of IFT trains is completed within ~1.3 s, with an ~1.7 s average waiting time between the departures of successive trains that contain complexes from the same anterograde train. These results are consistent with tip turnaround times measured previously for IFT subunits and axonemal cargoes (Craft et al., 2015; Qin et al., 2007; Reck et al., 2016; Wren et al., 2013). The analysis of the tip dwell times under different experimental conditions revealed that disassembly of anterograde trains and reassembly of the retrograde trains is a multistep process regulated by extracellular calcium, kinase activity, and the concentration of active dynein motors.

Simultaneous tracking of the KAP subunit of kinesin-2 and the LIC subunit of dynein-2 revealed how these motors are recycled back and forth within a flagellum. Kinesin-2 powers anterograde trains and dissociates from the IFT trains at the tip. KAP returns to the flagellar base by diffusing within the flagellum, similar to the diffusion of kinesin-1 in mammalian neurons (Blasius et al., 2013). We propose that the diffusion of KAP represents the entire heterotrimeric kinesin-2 complex because KAP and the kinesin-2 motor subunits co-sediment in sucrose density gradients of purified flagella extracts (Cole et al., 1998; Mueller et al., 2005) and neither KAP nor FLA10 accumulate in flagella during inactivation of retrograde transport (Engel et al., 2012; Pedersen et al., 2006). Diffusion may also play a role in recycling other components to the cell body. During flagellar disassembly, removal of flagellar components occurs independently of IFT (Stephens, 2000), presumably in a manner similar to kinesin-2.

Dynein-2 moves to the tip in association with anterograde trains (Reck et al., 2016). Because only kinesin motors remain active during anterograde IFT (Shih et al., 2013), we concluded that dynein-2 is carried as an inactive passenger and it actively engages with microtubules when it reaches to the flagellar tip (Figure 4d). The average tip turnaround time of dynein-2 is similar to

kinesin-2 (Welch's t test, $p = 0.05$), and the initiation of retrograde transport does not require departure of kinesin-2 motors from the tip.

These results differ considerably from the studies of certain mammalian and nematode cilia, in which two different kinesin-2 motors cooperate during anterograde IFT (Broekhuis et al., 2014; Prevo et al., 2015; Williams et al., 2014). For example, in mouse olfactory sensory neurons, heterotrimeric kinesin-2 is capable of moving IFT particles along both middle and distal segments of the cilium independently of homodimeric Kif17 (Williams et al., 2014). In *C. elegans*, kinesin-2 and OSM-3 function redundantly along the axoneme's middle segment, while OSM-3 alone transports IFT particles on the distal segment (Snow et al., 2004). These kinesin-2 motors were observed to move in retrograde directions. Unlike studies on *C. elegans*, we did not observe frequent pausing of anterograde trains and reversal of kinesin-2 and dynein-2 motors along the length of the cilium (Mijalkovic et al., 2017; Prevo et al., 2015). Most of the reversals occur at the flagellar tip, and reversal of particles before reaching the tip is rare in *Chlamydomonas* flagella (Dentler, 2005). In addition, we did not observe acceleration and deceleration of IFT trains near the turnaround zones, nor instantaneous reversal of dynein-2 at the ciliary tip (Mijalkovic et al., 2017; Prevo et al., 2015). The reasons for these differences in IFT dynamics and turnover remain unknown and may be related to variations in ciliary structure and organization, phosphorylation of kinesin-2 motors (Liang et al., 2014), and posttranslational modification of the microtubule tracks (Stepanek and Pigino, 2016).

Kinesin-2 returns from the ciliary tip to the cell body by diffusion

Dissociation of KAP from IFT trains at the tip is consistent with the recycling of kinesin-2 to the cell body in the absence of active retrograde IFT (Pedersen et al., 2006). However, it remained unclear how kinesin-2 achieves this long-range movement without active transport. To test

257 whether diffusion from the tip effectively recycles KAP to the cell body, we performed
258 fluorescence recovery after photobleaching (FRAP) assays in the middle sections of full-length
259 flagella of *fla3*::KAP-GFP cells (~12 µm, Figure 5a, Video 8). Directional movements of KAP-
260 GFP labeled trains into the photobleached area were seen from the anterograde direction,
261 whereas recovery of GFP fluorescence from the retrograde direction was primarily due to
262 diffusion of KAP-GFP from the tip. These results suggest that the high fluorescent background
263 seen in KAP-GFP flagella was caused by kinesin-2 motors dissociated from IFT trains at the tip.
264 The diffusion constant calculated from the fluorescence recovery (1.8 ± 0.1 µm^2 s^{-1}, Figure 5b)
265 was similar to the result of the MSD analysis (Figure 3h). Fluorescent background in KAP-GFP
266 flagella increased towards the tip, suggesting an efflux of diffusing KAP-GFP towards the cell
267 body (Figure 5c,d). During flagellar regrowth, the KAP-GFP gradient was maintained for all
268 flagellar lengths (Figure 5-figure supplement 1a, see Materials and Methods). The influx of
269 KAP-GFP fluorescence from the base to the flagellum through anterograde IFT was statistically
270 indistinguishable from the estimated efflux of KAP-GFP to the base through one-dimensional
271 diffusion in flagella (Welch's t-test, $p = 0.80$, $N = 57$, Figure 5-figure supplement 2, see Materials
272 and Methods). These results strongly indicate that KAP-GFP returns to the cell body by diffusing
273 from the flagellar tip.

274 We ran Monte Carlo simulations to estimate the accumulation of KAP in a flagellum in a steady-
275 state using the measured values of IFT train loading (Engel et al., 2009), diffusion coefficient,
276 flagellar length, and IFT train frequency. The model assumes that KAP is released from
277 anterograde IFT trains at the tip, diffuses within a flagellum, and is taken up by the basal body.
278 Under these conditions, simulations confirmed the build-up of a linear concentration gradient of
279 KAP in the flagellum (Figure 5-figure supplement 1b). In fully-grown flagella, the return of KAP

to the flagellar base takes 42 s on average, an order of magnitude longer than the travel of retrograde trains (4 s) to the base. This delay leads to a ~4-fold higher amount of KAP inside the flagellum compared to a case in which KAP returns to the base with retrograde trains (Figure 5-figure supplement 1c). Unlike KAP, IFT27 has low fluorescence background without an obvious concentration gradient along the length of the flagellum (Figure 5d) due to active transport of the IFT trains in both directions.

Kinesin-2 is depleted from the basal body during flagellar regrowth

KAP-GFP loading on IFT particles has been shown to decrease with increasing flagellar length (Engel et al., 2009), but the underlying mechanism remained unclear. We reasoned that, as the flagella elongate, diffusion of KAP from the tip to the base takes a longer time and a larger amount of KAP builds up in the flagellum. This may deplete the amount of KAP available at the flagellar base and lead to decreased loading of KAP onto the subsequent IFT trains. To test this model, we deflagellated *fla3::*KAP-GFP cells and measured the GFP fluorescence at the basal body and in the flagellum at various times during flagellar regrowth using confocal microscopy (Figure 6a). We estimated that the total amount of KAP localized to the base and flagellum increased by two-fold with flagellar length, indicating the upregulation of IFT components during flagellar growth. The fluorescence intensity at the flagellar base was highest for short flagella (1-4 μm) and decreased ~4-fold as cells have grown full-length flagella (~10 μm, Figure 6b), significantly larger than ~1.6-fold reduction reported previously (Ludington et al., 2015). We also observed that the KAP fluorescence in the flagellum was low in short flagella and increased ~10-fold as the flagellar length reached the steady-state (Figure 6b).

Changes in the amount of IFT complexes were markedly different from that of KAP during flagellar regrowth (Figure 6a). In IFT20::IFT20 GFP cells, the GFP signal in the flagellum

303 increased with flagellar length (Figure 6c). This is in contrast to the previous reports showing
304 that total amount of IFT components remains constant during flagellar regeneration (Marshall
305 and Rosenbaum, 2001), but agrees with the proportional reduction in the IFT train size with
306 flagellar length (Engel et al., 2009). Unlike KAP-GFP, basal body fluorescence of IFT20-GFP
307 remained nearly constant across all flagellar lengths (Figure 6c). We concluded that depletion at
308 the base and accumulation in the flagella were not observed for IFT complexes because they are
309 rapidly returned to the base through active transport.

310 **Discussion**

311 Cilia and flagella serve as a model system to study how cells precisely control organelle size
312 because they elongate only in one direction. According to the balance point model, flagellar
313 length is set when flagellar assembly and disassembly rates reach equilibrium (Marshall et al.,
314 2005). While the disassembly rate is independent of flagellar length (Kozminski et al., 1995), the
315 assembly rate is determined by the injection of IFT trains. The amount of material being
316 transported by these trains to the tip is correlated strongly with the amount of material localized
317 to the flagellar base (Ludington et al., 2013, 2015; Wren et al., 2013), which serves as a loading
318 dock. Previous studies showed that IFT train size and the number of ciliary cargos per train
319 scales inversely with flagellar length (Craft et al., 2015; Engel et al., 2009), but it remained
320 unclear which essential component of the IFT machinery limits the assembly of IFT trains as the
321 flagellum elongates (Rosenbaum et al., 1969).

322 We propose that dissociation of kinesin-2 from IFT trains serves as a negative feedback
323 mechanism to control the length of *Chlamydomonas* flagella (Ludington et al., 2015). Our results
324 show that the majority of kinesin-2 dissociates from IFT trains at the flagellar tip and diffuses
325 within the flagellum. Diffusion leads to a large accumulation of kinesin-2 in the flagellum (Craft

et al., 2015) as the flagellum grows longer, while the amount of kinesin-2 at the base decreases several-fold. As a result, lower amounts of kinesin-2 are available to bring new anterograde IFT trains to the flagellar tip. This may lead to a reduction in the IFT train size and the rate of flagellar assembly as the flagella grow longer (Figure 6d,e).

Consistent with this model, previous studies showed that KAP intensity at the basal body correlates with KAP loading on IFT trains and the assembly rate during flagellar regeneration (Ludington et al., 2013). In the temperature-sensitive mutant strain *fla10*^{ts}, inactivation of kinesin-2 motility ceases IFT and leads to resorption of the flagellum at a constant rate (Kozminski et al., 1995; Marshall et al., 2005). At intermediate temperatures, flagellar length correlates strongly with the estimated fraction of active kinesin-2 motors in *fla10*^{ts} cells (Marshall and Rosenbaum, 2001), indicating that the amount of active kinesin-2 limits flagellar growth. Unlike kinesin-2, IFT components are rapidly recycled to the cell body by dynein-2 and the amount of these components at the flagellar base remains nearly constant as the flagellum elongates. Therefore, the abundance of IFT components at the flagellar base is not limiting to maintain flagellar length, and the cells grow full length flagella upon partial knockdown of IFT components (Qin et al., 2007).

Diffusion is also proposed to play a role in setting the length of bacterial flagella (Renault et al., 2017), long polymers made from a single protein flagellin. Similar to the flagellar length control model originally proposed for *Chlamydomonas* (Levy, 1974), flagellins are injected into the channel of the filament and they diffuse to reach the assembly site at the filament tip, generating a concentration gradient decreasing towards the tip. As the filament gets elongates, it grows more slowly because it takes longer for the components to reach the tip. In contrast to bacterial flagellin, structural components are carried to the tip by IFT in eukaryotic flagella. In

Chlamydomonas, diffusion of kinesin-2 from the tip sets a concentration gradient decreasing towards the basal body and its return to the flagellar base is delayed as the flagellum gets longer.

While kinesin-2 diffusion can account for setting the equilibrium length in the balance-point model (Ludington et al., 2015), other mechanisms must also exist to control assembly and disassembly of *Chlamydomonas* flagella (Pan et al., 2004). Our results show that IFT components are upregulated and they accumulate in large numbers at the flagellar base after deflagellation (Lefebvre and Rosenbaum, 1986). A large pool of IFT components in the cytoplasm partially exchanges with the flagellar pool (Buisson et al., 2013; Engel et al., 2009), because cells can grow half-length flagella after deflagellation under complete inhibition of protein synthesis (Rosenbaum et al., 1969). The mechanisms that control the expression of IFT components after deflagellation, regulate the exchange of material between the basal body and cytoplasm, and load material onto IFT trains remain poorly understood. Further studies in mutant cell lines that have abnormally long (Nguyen et al., 2005; Tam et al., 2007) or short flagella may also reveal which proteins specifically regulate these processes.

Materials and Methods

Strains and cell culture

The *pf18 IFT27-GFP* strain was obtained from the Marshall laboratory (University of California San Francisco) after crossing the *IFT27-GFP* transgene into the *pf18* background as previously described (Engel et al., 2009; Qin et al., 2007). The *ift20::IFT20-GFP* strain (Lechtreck et al., 2009) was obtained from the Lechtreck laboratory (University of Georgia). The *fla3::KAP-GFP* (Mueller et al., 2005) and *d1blic::D1bLIC-GFP* (Reck et al., 2016) strains are available from *Chlamydomona*s Resource Center at the University of Minnesota. The *d1blic*::*D1bLIC-crCherry KAP-GFP* strain was generated as described below. Strains were maintained on plates of TAP media containing 1% agar. For light microscopy, vegetative cells were resuspended in liquid TAP media at 22 ºC for 24-48 hours and passaged to fresh liquid TAP before introducing into a flow chamber.

Isolation and characterization of the *d1blic::D1bLIC-crCherry KAP-GFP* strain.

The *D1bLIC-crCherry* construct was generated by subcloning a *Chlamydomonas* codon optimized version of the Cherry tag into a genomic copy of the *D1bLIC* gene (Reck et al., 2016). The Cherry tag was amplified by PCR from the plasmid pBR9 mCherryCr (Rasala et al., 2013) and inserted into a unique *Asc*I site located in the last exon of *D1bLIC*. The D1bLIC-crCherry construct was linearized with *Bam*HI and co-transformed into *d1blic* (CC-4487) with the selectable marker pSI103 and plated on TAP medium plus 10 μg/ml paromomycin. 960 transformants were picked into TAP media and screened for changes in colony morphology. 84 colonies were further examined by both phase contrast and fluorescence microscopy for rescue of flagellar assembly and expression of Cherry. Isolated flagella from four colonies were analyzed by Western blot for the presence of full-length D1bLIC-Cherry. A single colony was

selected for a second round of transformation using the *KAP-GFP* construct (Mueller et al., 2005) and the plasmid pHyg3 (Berthold et al., 2002) and selection on 10 µg/ml of hygromycin B. Two out of 96 transformants were identified as positive for both GFP and Cherry by fluorescence microscopy, and Western blots of isolated flagella confirmed the presence of both D1bLIC-Cherry and KAP-GFP in the rescued strains. Antibodies used included a rat antibody against *Chlamydomonas* KAP (Mueller et al., 2005), a mouse antibody against GFP (Covance, Inc.), a rabbit antibody against *Chlamydomonas* D1bLIC (Perrone et al., 2003), and a rabbit antibody against mCherry (Rockland Immunochemicals).

Drug treatment

0.34 mM Ca^{2+} in TAP media was depleted by adding 0.5 mM EGTA, which resulted a free Ca^{2+} concentration of 1.5 µM. The concentration of free Ca^{2+} in the assay buffer as a function of added EGTA was calculated from the Chelator program (http://maxchelator.stanford.edu). For drug treatment assays, a final concentration of 0.1 mM ciliobrevin D, 5 mM db-cAMP and IBMX, or 1 mM kinase inhibitor H-8 was added to the TAP media, and the data was collected 5-10 minutes after the treatment.

Deflagellation and flagellar regrowth

For imaging the diffusion gradient in live *fla3::KAP-GFP* cells, we deflagellated cells in TAP media using shear force by rapidly pushing them through a 20G1 ½ syringe. Cells regenerating flagella were imaged in the following hour. For imaging the accumulation of GFP signal at the basal body region and in regenerating flagella, fla*3::KAP-GFP* and *IFT20::IFT20-GFP* cells were deflagellated with pH shock by adding 60 µl 0.5 N acetic acid to 1 ml of cells in TAP media, waiting 45 seconds, and adding 60 µl 0.5 N KOH. Cells were fixed 15, 30, 45, 60, and 75 minutes after pH shock. Fixation was done by pipetting 200 µl of liquid TAP cell culture onto a

poly-lysine treated coverslip for 1 minute, then gently treating the coverslip with 4% paraformaldehyde in water for 10 min. Afterwards, the coverslip was treated twice with 100% methanol chilled to -20 ℃ for 5 minutes. Coverslips were dipped in water to remove methanol, mounted in a flow chamber with TAP media, and then imaged immediately.

TIR microscopy

A custom-built objective-type TIR fluorescence microscope was set up, using a Nikon TiE inverted microscope equipped with a perfect focusing unit, bright-field illumination, and a 100X 1.49 NA PlanApo oil immersion objective (Nikon). 488 nm and 561 nm solid state lasers (Coherent) were used for GFP and crCherry excitation, respectively. The angle of incident light was adjusted lower than the critical angle to illuminate a deeper field (~300 nm) near the coverslip surface. The fluorescent signal was recorded by an Andor iXon 512 x 512 electron-multiplied charge-coupled device (EM-CCD) camera. 1.5x extra magnification was used to obtain an effective pixel size of 106 nm. Data was collected at 10 Hz. Excitation laser beams were controlled by shutters (Uniblitz). Because the CCD image saturates under intense laser illumination of the focused gate beam, shutter timing was synchronized with the camera acquisition by a data acquisition card (NI, USB-6221) to minimize the number of saturated frames in recorded movies. For two-color imaging, GFP and crCherry fluorescence were separated into two channels on a CCD using Optosplit II (Cairn). To avoid bleed-through between channels, movies were acquired using a time-sharing between 488 nm and 561 nm laser beams, synchronized with camera acquisition at 60 ms frame time. The effective pixel size was 160 nm.

PhotoGate assays

PhotoGate assays were performed as previously described(Belyy et al., 2017). Briefly, a 488-nm

laser beam was split into two paths using a half-wave plate and a polarizer beamsplitter cube. The first path was used for objective-type TIRF imaging. The second path was focused (2 MW cm^{-2}) to the image plane and steered with a fast piezo-driven mirror (S-330.8SL, Physik Instrumente). The piezo-driven mirror was mounted at a position conjugate to the back-focal plane of the objective to ensure that the tilting of the mirror resulted in pure translation of the focused beam in the image plane. The mirror provided a usable travel range of 30 µm x 30 µm area at the image plane. The mirror's angle was updated via analog output channels of a data acquisition card (NI, USB-6221) and controlled by software custom-written in LabVIEW.

Flagellar orientation of surface adhered cells was visualized by TIRF imaging. Initially, the gate beam was placed at the tip of flagellum and moved along the flagellar orientation to prebleach the distal half of the flagellum. The gate beam was turned off when it was positioned near the base of the flagellum to allow a single fluorescent anterograde train to enter the flagellum. Occasionally (<5%), two anterograde trains overlapped and entered the flagellum simultaneously. The gate beam was then turned on for 0.2 s of every 1 s to bleach other anterograde trains. Under these conditions, less than 1% of anterograde IFT trains moved faster than the cutoff speed (3.0 µm s^{-1}) and were able to escape the gate. The trajectories of these trains can be distinguished from each other as they move at different speeds along the flagellum. The locations of flagellar tips were determined by brightfield imaging (data not shown). In two-color photogate experiments, the focused 488-nm laser beam was used to bleach both GFP and crCherry and 488 and 561 beams were used in a time-sharing mode for TIR excitation.

FRAP assays

FRAP assays on the *fla3::*KAP-GFP strain were performed by photobleaching the center part of the flagellum (5 µm in length) for 200 ms at 25 kW cm^{-2} in the epifluorescence mode. The

recovery of fluorescence signal in the bleached area was simultaneously monitored by imaging with a 100 W cm^{-2} TIRF excitation. The analysis was performed by measuring the total fluorescence intensity within the bleached area. Fluorescent signal of anterograde transport was manually excluded from the analysis. 13 different recovery traces were used in the MSD analysis. The intensity of each trace was normalized according to the initial and final intensity.

Confocal microscopy

fla3::KAP-GFP and *IFT20::IFT20-GFP* cells were fixed with paraformaldehyde at 15, 30, 45, 60, and 75 min intervals after deflagellation, as described above. The sample was imaged on a Zeiss confocal microscope using 488 nm laser excitation. Images were recorded with 560 nm *z* step, 63 nm pixel size, and 1.58 µs photon collection per pixel. Fluorescence in basal body and flagellum was quantified using ImageJ. The ratio of flagellar to basal-body KAP-GFP fluorescence in confocal images was similar to that of images recorded with TIR excitation, indicating that the fixation protocol did not result in the loss of diffusing KAP-GFP signal from the flagella. We confirmed that fixation did not alter the relative amount of KAP-GFP in the flagellum and the base by comparing the flagellum to base fluorescence ratio in live and fixed *fla3::*KAP-GFP cells.

Data analysis

Anterograde and retrograde trajectories were manually assigned from kymographs. After the arrival of a single anterograde particle at the tip, the departure of fluorescent retrograde trains was determined at a single pixel and frame resolution. The tip return time for each retrograde train was defined as the duration between the arrival of the fluorescent anterograde train and the departure of the retrograde train from the tip. Tip return time histograms were constructed and fitted to a Gamma function using MATLAB. The Gamma function was defined as $\Gamma(t) = t^{\alpha-1}e^{-\lambda t}$,

where α and λ are shape and rate parameters, respectively.

For single particle tracking analysis, the positions of fluorescent spots were determined by fitting the PSFs to a 2D Gaussian. The positions were fitted throughout the movie except at the frames when the gate beam was on or the frames in which the tracked particle overlapped with other fluorophores. The intensity of the fluorescent spots was estimated by the volume of the 2D Gaussian peak. In a typical assay, we adjusted excitation power to achieve 20-nm localization accuracy at 10 Hz image acquisition rate. Individual GFP spots were tracked for 5 s on average before photobleaching and diffusion constant was obtained by the MSD analysis of individual spots.

To determine the distribution of the KAP-GFP background in flagella, anterograde trajectories in kymographs of *fla3::*KAP-GFP cells were manually removed using custom ImageJ plugins. The remaining pixels were averaged over the kymograph's time axis, giving a time-averaged plot of the KAP-GFP background over the flagellum length. The cells were grouped by flagellar length. The background intensity and flagellum length of each cell were normalized. The average background intensity along the length of the flagellum was calculated for each group of cells.

KAP-GFP efflux from the flagellum was calculated using Fick's law. The slope of the KAP-GFP background over the length of a flagellum was multiplied by the diffusion constant (1.7 $\mu m^2 s^{-1}$). To calculate KAP-GFP influx, the KAP-GFP background was subtracted from the kymographs. Then, the average intensity of anterograde trains was multiplied by the train frequency (1.3 trains s^{-1}) to calculate the influx.

Monte Carlo simulations

Monte Carlo simulations were performed to test the effect of limited number of GFPs per train

and GFP photobleaching in PhotoGate experiments using the *pf18 IFT27-GFP* strain. Experimentally measured values were used for the velocity and frequency of anterograde and retrograde trains. Simulations assumed that retrograde trains depart from the tip through a purely stochastic process, with two distinct rates determined in the experiments.

We estimated that each anterograde train contains 6 fluorescent GFPs by comparing the fluorescent intensities of anterograde trains in the *pf18 IFT27-GFP* strain to those of KAP-GFP spots in the *fla3::KAP-GFP* strain under the same imaging conditions and calibrating the number of molecules based on previous photobleaching analysis of the *fla3::KAP-GFP* strain[36]. Each retrograde train was constructed by a random selection of IFT particles available at the tip. Tip intensity measurements revealed that the signal of the IFT complexes located at the tip is three times brighter than an average anterograde train. The photobleaching of GFPs (0.05 s^{-1}) under TIR illumination was accounted for in simulations and trains with at least one fluorescent GFP were marked detectable.

Simulations were also run to estimate the distribution of diffusing KAP molecules in the flagellum at a steady-state. In these simulations, previously reported values for the anterograde train injection rate (1.3 trains s^{-1}) (Mueller et al., 2005) and the average number of KAP bound to a single anterograde train for each flagellar length(Engel et al., 2009) were used to estimate the number of KAP that arrives at the flagellar tip per second. KAP dissociated from the trains at the tip and immediately started one dimensional diffusion in the flagellum. The remodeling time of KAP at the tip was insignificant, and was not accounted for. The flagellum was modeled as a 5 - 12 µm long linear grid with spacing defined as the MSD of KAP diffusing at 1.7 μm^2 s^{-1} (Figure 3h) during the time-step of the simulation (5 ms). At every time point, each active molecule had its grid position changed by +1 or -1. The molecules at the extreme terminus of the tip only

moved towards the base. The diffusing KAP molecules were perfectly absorbed to the cell body as they arrived at the flagellar base (i.e. perfect sink) and exited the simulation. The simulations were run for 100,000 time points to allow molecules to reach a steady-state. The number of molecules at each grid position was calculated to plot the distribution of KAP molecules diffusing along the length of the flagellum. The total number of KAP was calculated by integrating the number of KAP diffusing along the entire flagellum and KAP on the anterograde trains. This number was compared to a hypothetical scenario that KAP returns to the cell body with active transport. The simulations were run 10 times to calculate the error.

Data and code availability

All data and simulation code that support the conclusions are available from the authors on request.

References

Belyy, V., Shih, S.-M., Bandaria, J., Huang, Y., Lawrence, R.E., Zoncu, R., and Yildiz, A. (2017). PhotoGate microscopy to track single molecules in crowded environments. Nat. Commun. *8*, 13978.

Berthold, P., Schmitt, R., and Mages, W. (2002). An engineered Streptomyces hygroscopicus aph 7" gene mediates dominant resistance against hygromycin B in Chlamydomonas reinhardtii. Protist *153*, 401–412.

Blasius, T.L., Reed, N., Slepchenko, B.M., and Verhey, K.J. (2013). Recycling of Kinesin-1 Motors by Diffusion after Transport. PLoS One *8*, 45–49.

Broekhuis, J.R., Verhey, K.J., and Jansen, G. (2014). Regulation of cilium length and intraflagellar transport by the RCK-kinases ICK and MOK in renal epithelial cells. PLoS One *9*.

Brown, J.M., and Witman, G.B. (2014). Cilia and diseases. Bioscience *64*, 1126–1137.

Buisson, J., Chenouard, N., Lagache, T., Blisnick, T., Olivo-Marin, J.-C.J.-C., and Bastin, P. (2013). Intraflagellar transport proteins cycle between the flagellum and its base. J. Cell Sci. *126*, 327–338.

Cole, D.G., Diener, D.R., Himelblau, A.L., Beech, P.L., Fuster, J.C., and Rosenbaum, J.L. (1998). Chlamydomonas kinesin-II-dependent intraflagellar transport (IFT): IFT particles contain proteins required for ciliary assembly in Caenorhabditis elegans sensory neurons. J. Cell Biol. *141*, 993–1008.

Craft, J.M., Harris, J.A., Hyman, S., Kner, P., and Lechtreck, K.F. (2015). Tubulin transport by IFT is upregulated during ciliary growth by a cilium-autonomous mechanism. J. Cell Biol. *208*, 223–237.

Dentler, W. (2005). Intraflagellar transport (IFT) during assembly and disassembly of Chlamydomonas flagella. J. Cell Biol. *170*, 649–659.

Engel, B.D., Ludington, W.B., and Marshall, W.F. (2009). Intraflagellar transport particle size scales inversely with flagellar length: Revisiting the balance-point length control model. J. Cell Biol. *187*, 81–89.

Engel, B.D., Ishikawa, H., Wemmer, K. a., Geimer, S., Wakabayashi, K.I., Hirono, M., Craige, B., Pazour, G.J., Witman, G.B., Kamiya, R., et al. (2012). The role of retrograde intraflagellar transport in flagellar assembly, maintenance, and function. J. Cell Biol. *199*, 151–167.

Harris, J.A., Liu, Y., Yang, P., Kner, P., and Lechtreck, K.F. (2016). Single-particle imaging

565 reveals intraflagellar transport-independent transport and accumulation of EB1 in
566 Chlamydomonas flagella. Mol. Biol. Cell *27*, 295–307.
567 Helenius, J., Brouhard, G., Kalaidzidis, Y., Diez, S., and Howard, J. (2006). The depolymerizing
568 kinesin MCAK uses lattice diffusion to rapidly target microtubule ends. Nature *441*, 115–119.
569 Iomini, C., Babaev-Khaimov, V., Sassaroli, M., and Piperno, G. (2001). Protein particles in
570 Chlamydomonas flagella undergo a transport cycle consisting of four phases. J. Cell Biol. *153*,
571 13–24.
572 Ishikawa, H., and Marshall, W.F. (2011). Ciliogenesis: building the cell's antenna. Nat Rev Mol
573 Cell Biol *12*, 222–234.
574 Kozminski, K.G., Johnson, K. a, Forscher, P., and Rosenbaum, J.L. (1993). A motility in the
575 eukaryotic flagellum unrelated to flagellar beating. Proc. Natl. Acad. Sci. U. S. A. *90*, 5519–
576 5523.
577 Kozminski, K.G., Beech, P.L., and Rosenbaum, J.L. (1995). The Chlamydomonas kinesin-like
578 protein FLA10 is involved in motility associated with the flagellar membrane. J. Cell Biol. *131*,
579 1517–1527.
580 Laib, J.A., Marin, J.A., Bloodgood, R.A., and Guilford, W.H. (2009). The reciprocal
581 coordination and mechanics of molecular motors in living cells. Proc Natl Acad Sci U S A *106*,
582 3190–3195.
583 Lechtreck, K.-F., Johnson, E.C., Sakai, T., Cochran, D., Ballif, B. a, Rush, J., Pazour, G.J., Ikebe,
584 M., and Witman, G.B. (2009). The Chlamydomonas reinhardtii BBSome is an IFT cargo
585 required for export of specific signaling proteins from flagella. J. Cell Biol. *187*, 1117–1132.
586 Lechtreck, K.F., Van De Weghe, J.C., Harris, J.A., and Liu, P. (2017). Protein transport in
587 growing and steady-state cilia. Traffic.
588 Lefebvre, P. a, and Rosenbaum, J.L. (1986). Regulation of the synthesis and assembly of ciliary
589 and flagellar proteins during regeneration. Annu. Rev. Cell Biol. *2*, 517–546.
590 Levy, E.M. (1974). Flagellar elongation as a moving boundary problem. Bull. Math. Biol. *36*,
591 265–273.
592 Liang, Y., Pang, Y., Wu, Q., Hu, Z., Han, X., Xu, Y., Deng, H., and Pan, J. (2014). FLA8/KIF3B
593 Phosphorylation Regulates Kinesin-II Interaction with IFT-B to Control IFT Entry and
594 Turnaround. Dev. Cell *30*, 585–597.
595 Ludington, W.B., Wemmer, K. a, Lechtreck, K.F., Witman, G.B., and Marshall, W.F. (2013).

596 Avalanche-like behavior in ciliary import. Proc. Natl. Acad. Sci. U. S. A. *110*, 3925–3930.
597 Ludington, W.B., Ishikawa, H., Serebrenik, Y. V., Ritter, A., Hernandez-Lopez, R.A.,
598 Gunzenhauser, J., Kannegaard, E., and Marshall, W.F. (2015). A systematic comparison of
599 mathematical models for inherent measurement of ciliary length: How a cell can measure length
600 and volume. Biophys. J. *108*, 1361–1379.
601 Marshall, W.F., and Rosenbaum, J.L. (2001). Intraflagellar transport balances continuous
602 turnover of outer doublet microtubules: implications for flagellar length control. J. Cell Biol.
603 *155*, 405–414.
604 Marshall, W., Qin, H., Brenni, M., and Rosenbaum, J. (2005). Flagellar Length Control System:
605 Testing a Simple Model Based on Intraflagellar Transport and Turnover. Mol. Biol. Cell *16*, 270–
606 278.
607 Mijalkovic, J., Prevo, B., Oswald, F., Mangeol, P., and Peterman, E.J.G. (2017). Ensemble and
608 single-molecule dynamics of IFT dynein in Caenorhabditis elegans cilia. Nat. Commun. *8*,
609 14591.
610 Mueller, J., Perrone, C.A., Bower, R., Cole, D.G., and Porter, M.E. (2005). The FLA3 KAP
611 Subunit Is Required for Localization of Kinesin-2 to the Site of Flagellar Assembly and
612 Processive Anterograde Intraflagellar Transport. Mol. Biol. Cell *16*, 1341–1354.
613 Nguyen, R.L., Tam, L.W., and Lefebvre, P.A. (2005). The LF1 gene of Chlamydomonas
614 reinhardtii encodes a novel protein required for flagellar length control. Genetics *169*, 1415–
615 1424.
616 Pan, J., Wang, Q., and Snell, W.J. (2004). An aurora kinase is essential for flagellar disassembly
617 in Chlamydomonas. Dev. Cell *6*, 445–451.
618 Pazour, G.J., Dickert, B.L., and Witman, G.B. (1999). The DHC1b (DHC2) isoform of
619 cytoplasmic dynein is required for flagellar assembly. J Cell Biol *144*, 473–481.
620 Pedersen, L.B., Geimer, S., and Rosenbaum, J.L. (2006). Dissecting the molecular mechanisms
621 of intraflagellar transport in Chlamydomonas. Curr. Biol. *16*, 450–459.
622 Perrone, C.A., Tritschler, D., Patrick, T., Raqual, B., Yoder, B.K., and Porter, M.E.*‡ (2003). A
623 Novel Dynein Light Intermediate Chain Colocalizes with the Retrograde Motor for Intraflagellar
624 Transport at Sites of Axoneme Assembly in Chlamydomonas and Mammalian Cells. Mol. Biol.
625 Cell *14*, 2559–2569.
626 Pigino, G., Geimer, S., Lanzavecchia, S., Paccagnini, E., Cantele, F., Diener, D.R., Rosenbaum,

J.L., and Lupetti, P. (2009). Electron-tomographic analysis of intraflagellar transport particle trains in situ. J. Cell Biol. *187*, 135–148.

Porter, M.E., Bower, R., Knott, J.A., Byrd, P., and Dentler, W. (1999). Cytoplasmic dynein heavy chain 1b is required for flagellar assembly in Chlamydomonas. Mol. Biol. Cell *10*, 693–712.

Prevo, B., Mangeol, P., Oswald, F., Scholey, J.M., and Peterman, E.J.G. (2015). Functional differentiation of cooperating kinesin-2 motors orchestrates cargo import and transport in *C. elegans* cilia. Nat. Cell Biol. *17*, 1536–1545.

Qin, H., Wang, Z., Diener, D., and Rosenbaum, J. (2007). Intraflagellar transport protein 27 is a small G protein involved in cell-cycle control. Curr Biol *17*, 193–202.

Rasala, B.A., Barrera, D.J., Ng, J., Plucinak, T.M., Rosenberg, J.N., Weeks, D.P., Oyler, G.A., Peterson, T.C., Haerizadeh, F., and Mayfield, S.P. (2013). Expanding the spectral palette of fluorescent proteins for the green microalga Chlamydomonas reinhardtii. Plant J. *74*, 545–556.

Reck, J., Schauer, A.M., VanderWaal Mills, K., Bower, R., Tritschler, D., Perrone, C.A., and Porter, M.E. (2016). The role of the dynein light intermediate chain in retrograde IFT and flagellar function in Chlamydomonas. Mol. Biol. Cell *27*, 2404–2422.

Renault, T.T., Abraham, A.O., Bergmiller, T., Paradis, G., Rainville, S., Charpentier, E., Guet, C.C., Tu, Y., Namba, K., Keener, J.P., et al. (2017). Bacterial flagella grow through an injection-diffusion mechanism. Elife *6*, e23136.

Rompolas, P., Pedersen, L.B., Patel-King, R.S., and King, S.M. (2007). Chlamydomonas FAP133 is a dynein intermediate chain associated with the retrograde intraflagellar transport motor. J Cell Sci *120*, 3653–3665.

Rosenbaum, J.L., Moulder, J.E., and Ringo, D.L. (1969). Flagellar elongation and shortening in Chlamydomonas. The use of cycloheximide and colchicine to study the synthesis and assembly of flagellar proteins. J. Cell Biol. *41*, 600–619.

Satir, P., Pedersen, L.B., and Christensen, S.T. (2010). The primary cilium at a glance. J. Cell Sci. *123*, 499–503.

Shih, S.M., Engel, B.D., Kocabas, F., Bilyard, T., Gennerich, A., Marshall, W.F., and Yildiz, A. (2013). Intraflagellar transport drives flagellar surface motility. Elife *2*, e00744.

Signor, D., Wedatman, K.P., Orozco, J.T., Dwyer, N.D., Bargmann, C.I., Rose, L.S., and Scholey, J.M. (1999). Role of a class DHC1b dynein in retrograde transport of IFT motors and IFT raft particles along cilia, but not dendrites, in chemosensory neurons of living Caenorhabditis

elegans. J. Cell Biol. *147*, 519–530.

Snow, J.J., Ou, G., Gunnarson, A.L., Walker, M.R.S., Zhou, H.M., Brust-Mascher, I., and Scholey, J.M. (2004). Two anterograde intraflagellar transport motors cooperate to build sensory cilia on C. elegans neurons. Nat. Cell Biol. *6*, 1109–1113.

Stepanek, L., and Pigino, G. (2016). Microtubule doublets are double-track railways for intraflagellar transport trains. Science (80-.). *352*, 721–724.

Stephens, R.E. (2000). Preferential incorporation of tubulin into the junctional region of ciliary outer doublet microtubules: A model for treadmilling by lattice dislocation. Cell Motil. Cytoskeleton *47*, 130–140.

Tam, L.W., Wilson, N.F., and Lefebvre, P.A. (2007). A CDK-related kinase regulates the length and assembly of flagella in Chlamydomonas. J. Cell Biol. *176*, 819–829.

Williams, C.L., McIntyre, J.C., Norris, S.R., Jenkins, P.M., Zhang, L., Pei, Q., Verhey, K., and Martens, J.R. (2014). Direct evidence for BBSome-associated intraflagellar transport reveals distinct properties of native mammalian cilia. Nat. Commun. *5*, 5813.

Wren, K.N., Craft, J.M., Tritschler, D., Schauer, A., Patel, D.K., Smith, E.F., Porter, M.E., Kner, P., and Lechtreck, K.F. (2013). A differential cargo-loading model of ciliary length regulation by IFT. Curr. Biol. *23*, 2463–2471.

Acknowledgments

We would like to thank K. Augsperger for assistance with the isolation and screening of the *D1bLIC-Cherry KAP-GFP* tagged strains, and V. Belyy, J. Bandaria, and P. Qin for technical assistance. This work has been supported by NIH (GM094522 (AY), GM055667 (MEP)), and NSF (MCB-1055017 and MCB-1617028 (AY)).

680 **Figures**

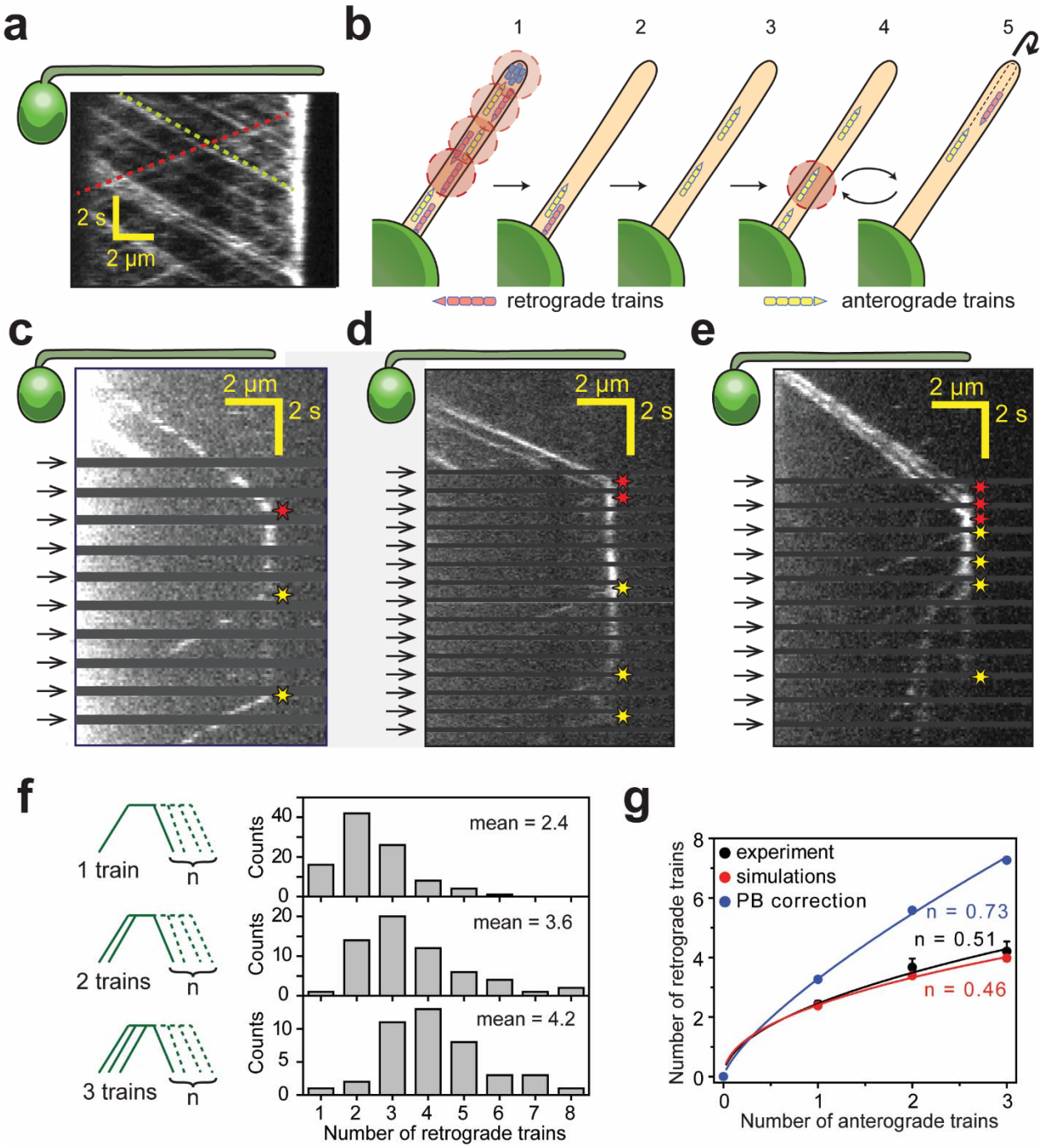

681

682 **Figure 1. IFT trains split apart and mix with each other at the flagellar tip.**

683 (**a**) Kymograph of a surface-immobilized *pf18 IFT27-GFP* strain shows that IFT trains move

684 bidirectionally along the flagellum, only reversing direction at the tip and the base. Multiple IFT

trains accumulate at the flagellar tip. Representative anterograde and retrograde trajectories are shown with yellow and red dashed lines, respectively. (**b**) Schematic representation of the PhotoGate assay. 1) The distal half of the flagellum is prebleached by moving the powerful gate beam from the flagellar tip to near the base of the flagellum. 2-3) The gate beam is turned off to allow a single anterograde train to enter the flagellum without photobleaching. 4) The beam is then repeatedly turned on to photobleach the successive trains entering the flagellum and 5) turned off for 0.8 s to image the single fluorescent train within the flagellum. Photobleached trains are not shown. (**c-e**) Kymographs of one (c), two (d) and three (e) fluorescent anterograde trains entering the flagellum. Anterograde trains pause at the flagellar tip and split into multiple retrograde trains that move back to the base. Arrival of fluorescent anterograde trains and departure of retrograde trains at the tip are shown with red and yellow stars, respectively. Arrows represent repetitive bleaching events near the base of the flagellum. **(f)** (Left) The number of fluorescent retrograde trains was quantified as a function of one, two or three fluorescent anterograde trains entering the flagellum after photobleaching. (Right) The average number of retrograde trains increased sub-proportionally with the number of fluorescent anterograde trains entering the flagellum. N = 97, 60, 42 train events from top to bottom, in 160 cells, from 13 independent experiments. **(g)** The number of detectable retrograde trains versus the numbers of incoming anterograde trains in PhotoGate experiments and Monte Carlo simulations (PB: photobleaching). Solid lines represent the fit of data to the power law ($y = ax^n$). n is less than 1 under each condition. Error bars represent s.e.m. (N = 5,000 for simulations).

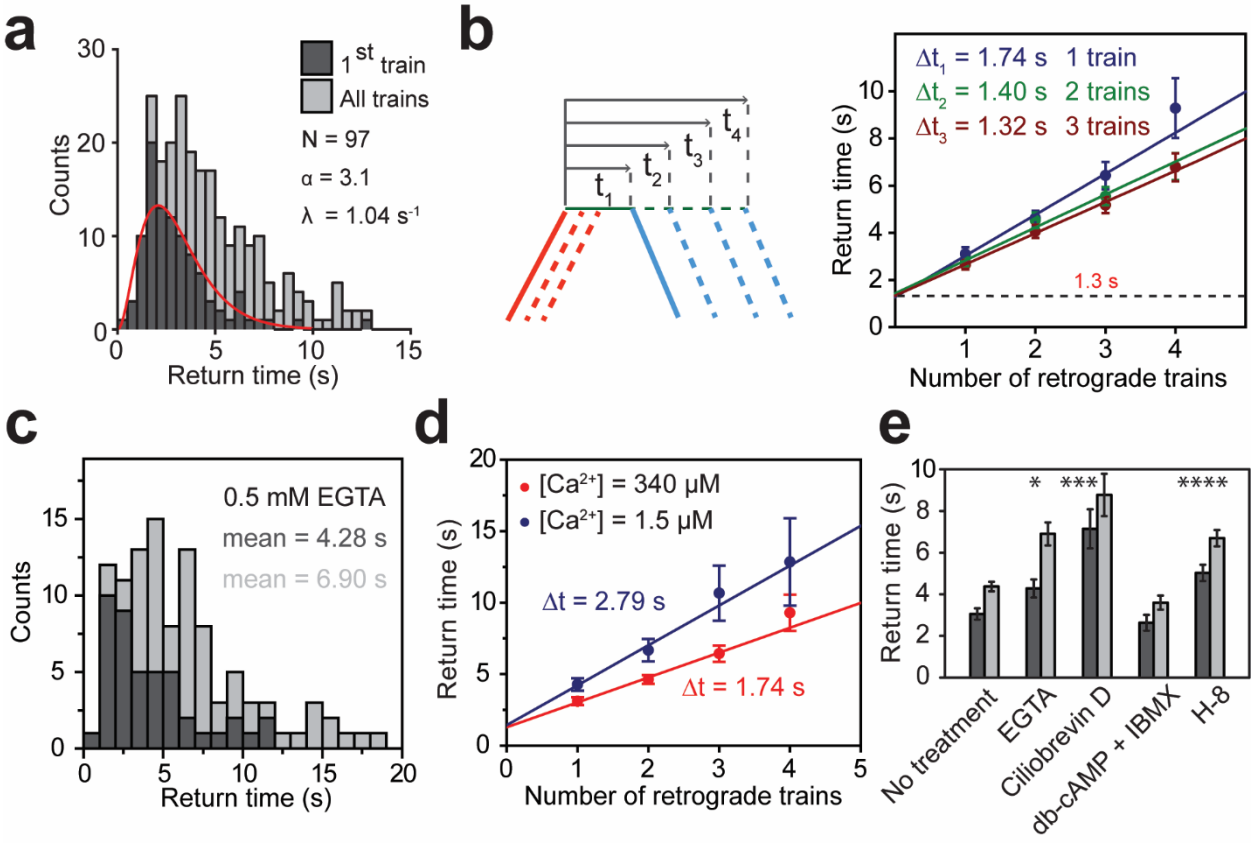

Figure 2. Tip turnaround of IFT trains is a multistep process regulated by dynein activity and extracellular Ca^{2+}.

(a) The tip return time histogram of the first retrograde IFT27-GFP train (dark grey) and all of the trains (light grey). The histogram of the first retrograde trains was fitted to a Gamma function (red curve). α and λ are shape and rate parameters, respectively. **(b)** (Left) The schematic shows the tip return time of the 1st, 2nd, 3rd and 4th retrograde IFT trains (t_1, t_2, t_3, t_4) emanating from one, two, and three fluorescent anterograde trains arriving at the tip. (Right) The linear fit to the average tip return time reveals that the time between successive trains (Δt) decreases by the number of anterograde trains, but the tip resting time (the y-intercept) remains constant (1.3 s). Error bars represent s.e.m. **(c)** The return time histogram of IFT27-GFP trains with EGTA treatment. N = 44 train events in 35 cells over 4 independent experiments. **(d)** Averaged return time of the 1st, 2nd, 3rd and 4th returning IFT27-GFP trains coming out of an anterograde train for

718 cells in TAP media (red, N = 97) and calcium-depleted media (blue, N = 44). Error bars represent
719 s.e.m. **(e)** IFT27-GFP return times in various drug treatments. N = 97, 44, 34, 34, 52 retrograde
720 trains from left to right, in a total of 22 independent experiments (*p < 0.05, ***p < 0.001, ****
721 p <0.0001, as compared to no treatment). In (a), (c) and (e), the first trains returning from the tip
722 are shown in dark grey and all trains are shown in light grey.

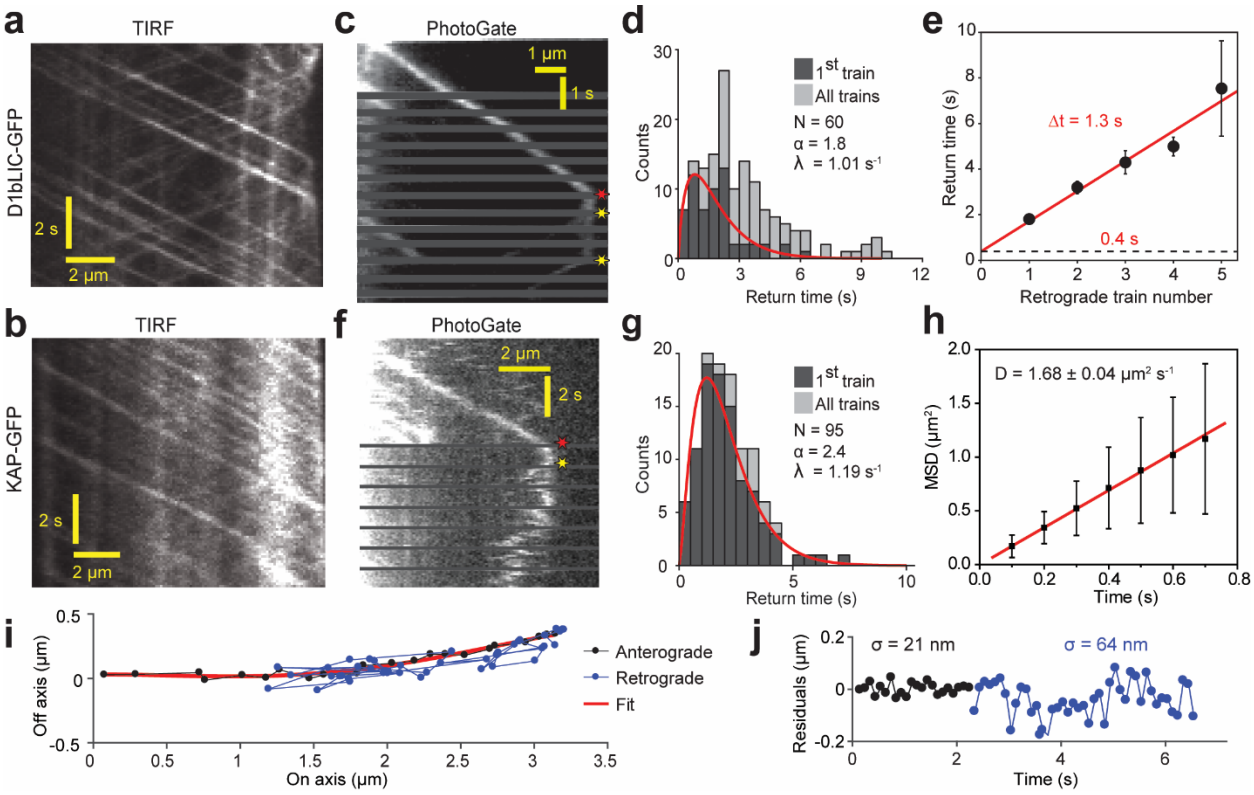

Figure 3. PhotoGate reveals the tip turnaround behavior of IFT motors.

(a) In a conventional TIR assay, anterograde and retrograde D1bLIC-GFP traces were clearly visible, but the tip behavior of individual trains could not be discerned. **(b)** In a conventional TIR assay, KAP-GFP was observed to move anterogradely, but the retrograde transport of KAP was rarely observed. **(c)** PhotoGate imaging of D1bLIC-GFP shows that D1bLIC trains move to the tip anterogradely, split into multiple trains, and return to the base retrogradely. Red and yellow stars indicate arrival to and departure of D1bLIC-GFP from the tip, respectively. **(d)** Tip return time histogram of D1bLIC-GFP. First train return times are fit to a gamma distribution (red curve) with shape (α) and rate (λ) parameters (mean ± 95% c.i.). N = 60 anterograde trains in 60 cells over 9 independent experiments. **(e)** Averaged return time of the 1st, 2nd, 3rd, 4th, and 5th D1bLIC-GFP particles returning from the tip (mean ± s.e.m.). **(f)** Kymograph analysis of a KAP-GFP cell imaged by PhotoGate. KAP undergoes active transport in the anterograde direction,

736 pauses at the flagellar tip, and diffuses back to the flagellar base. Arrows indicate the bleaching
737 events. **(g)** KAP-GFP return time histogram. The red curve represents a fit of first train return
738 times to a Gamma distribution. N = 95 anterograde trains in 47 cells over 4 independent
739 experiments. **(h)** MSD analysis of KAP-GFP movement after it leaves the flagellar tip. The
740 average diffusion constant is 1.68 ± 0.04 $\mu m^2\ s^{-1}$ (N = 27, mean ± s.e.m.). **(i)** High-resolution
741 tracking of a KAP-GFP particle reveals the two-dimensional trajectory during anterograde
742 (black) and diffusion (blue). The red curve is the polynomial fit to the trace. **(j)** The residual plot
743 to the trace in (h) reveals lateral fluctuations during anterograde transport (black) and diffusive
744 (blue) movement.

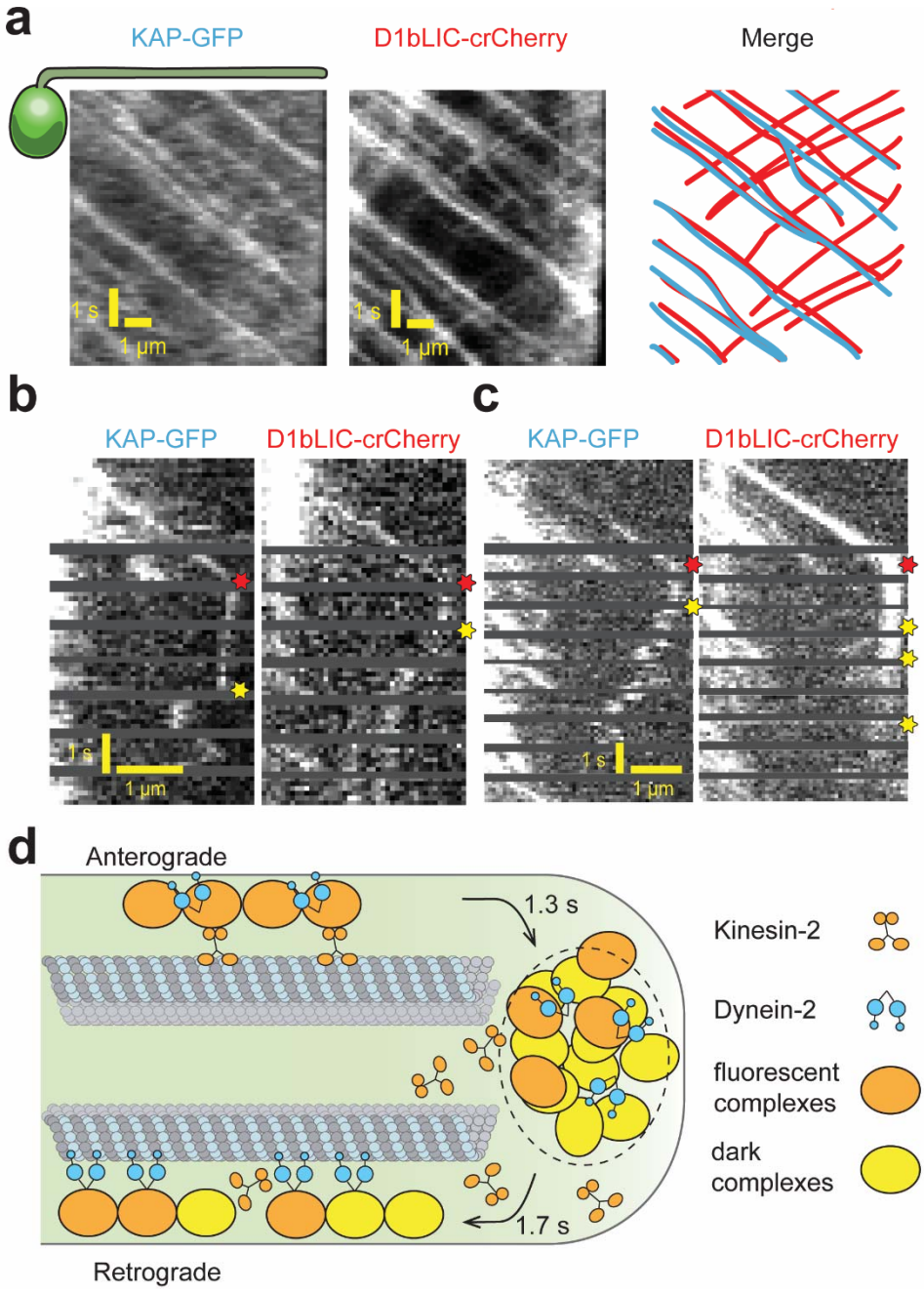

745

746 **Figure 4. Transport roles of kinesin-2 and dynein-2.**

747 **(a)** Representative kymographs of KAP-GFP and D1bLIC-crCherry in a *d1blic*::*D1bLIC-*
748 *crCherry KAP-GFP* flagellum. KAP-GFP and D1bLIC-crCherry co-localize on the IFT trains in
749 the anterograde direction. Retrograde tracks are seen in the D1bLIC-crCherry channel, but are
750 rarely visible in the KAP-GFP channel. (**b, c**) Two-color PhotoGate traces of KAP-GFP (left) and

751 D1bLIC-crCherry (right) in single flagella. KAP-GFP and D1bLIC-crCherry arrive at the tip on
752 the same train. In (b), D1bLIC leaves the tip before KAP. In (c), KAP diffuses away from the tip
753 before the departure of D1bLIC trains. Red and yellow stars indicate arrival to and departure
754 from the flagellar tip, respectively. (**d**) A model for the turnover of IFT trains and motors at the
755 flagellar tip. Kinesin-2 motors transport individual anterograde IFT trains to the flagellar tip.
756 Dynein-2 is carried with anterograde trains as an inactive passenger. At the tip, IFT complexes
757 detach from microtubules, disassemble, and mix with the tip protein pool to assemble new trains.
758 These trains are transported retrogradely by dynein-2. Kinesin-2 detaches from IFT trains at the
759 flagellar tip and diffuses back to the base by diffusion.

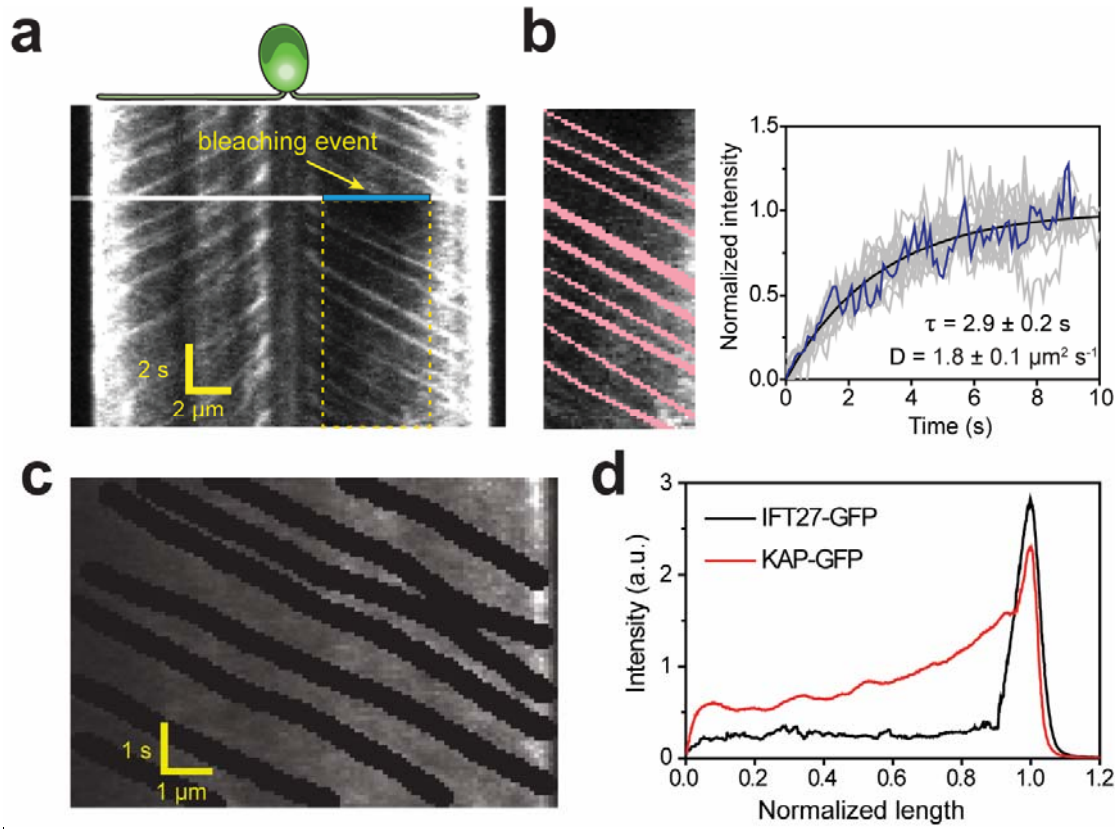

Figure 5. Diffusion of KAP from the flagellar tip leads to a concentration gradient along the flagellum.

(a) Kymograph of KAP-GFP movement before and after photobleaching the middle section of the flagellum (blue area). While fluorescence recovery from the base is through anterograde movement, the recovery from the tip region is due to diffusion. **(b)** (Left) The GFP signal of anterograde traces (red) was manually subtracted from the rectangular area shown in (a). (Right) The intensity in the photobleached area shows recovery as a function of time (blue line). The average recovery signal of 13 cells (grey lines) was fitted to a one-dimensional diffusion equation (black curve, ± 95% c.i.). **(c)** In conventional TIR imaging, anterograde trajectories of KAP-GFP were manually subtracted from the kymograph. **(d)** The average GFP signal along the length of a flagellum in KAP-GFP and IFT27-GFP cells after the removal of anterograde and retrograde transport traces from the kymographs. Flagellar base and tip positions were

normalized to 0 and 1, respectively. N = 11 for both KAP-GFP and IFT27-GFP.

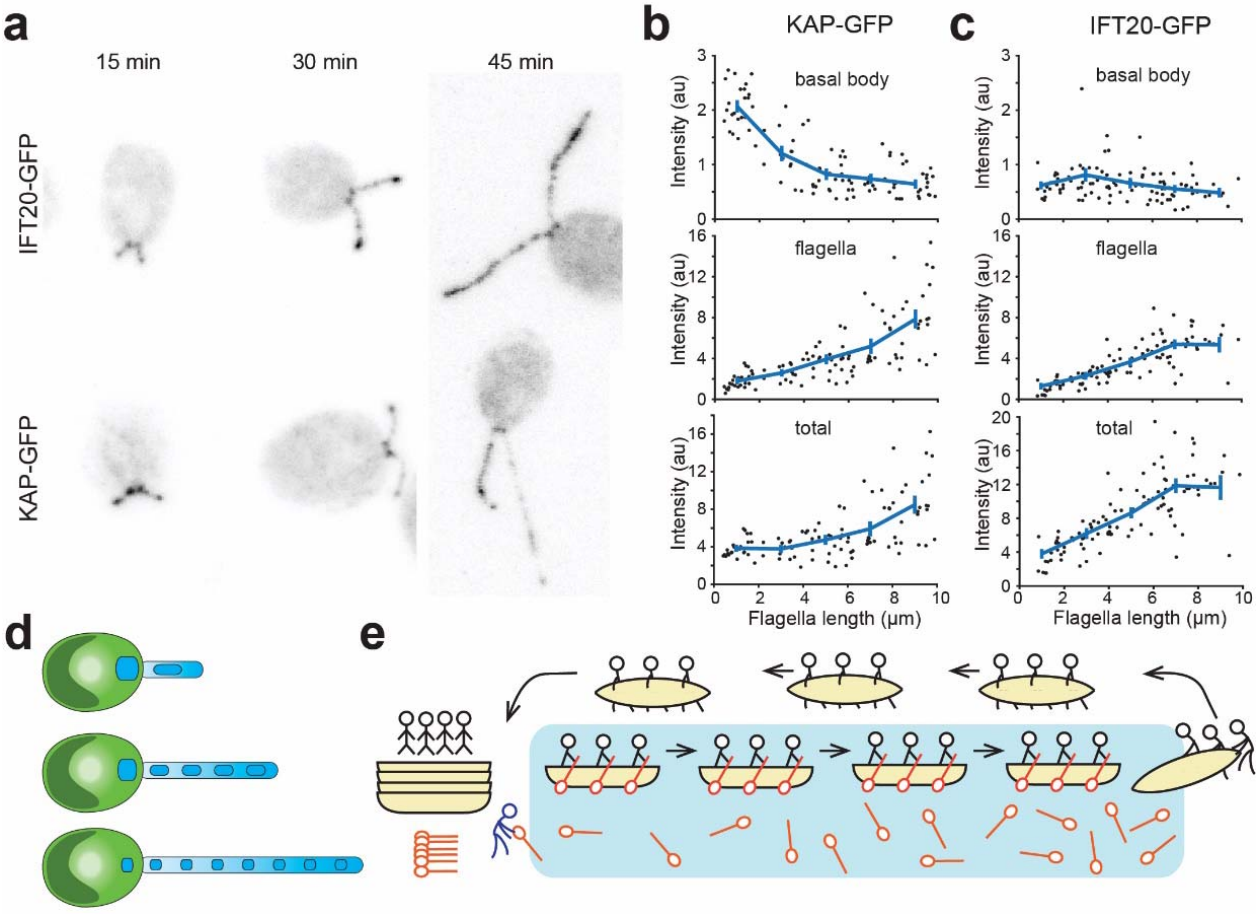

Figure 6. Kinesin-2 accumulates in flagella and is depleted at the basal body during flagellar growth.

(a) Representative confocal images show the distribution of IFT20-GFP and KAP-GFP fluorescence at the basal body region and in the flagella during flagellar regrowth. **(b,c)** Integrated KAP-GFP (b) and IFT20-GFP (c) fluorescence at the basal body (top), in the flagellum (middle), and in both regions (bottom) at different flagellar lengths. Each black dot represents a single cell and the blue line is the running average (±s.e.m.). For KAP-GFP, N = 104 flagella from 70 cells over 2 independent experiments. For IFT20-GFP, N = 103 flagella from 56 cells over 2 independent experiments. **(d)** A model for flagellar length control. When the flagellum is short, IFT trains contain more kinesin-2 from the large basal body pool. As flagella

785 elongate, the number of kinesin-2 per IFT train decreases because a significant fraction of the
786 kinesin-2 unloads at the tip and undergoes diffusion in the flagellar lumen, depleting the kinesin-
787 2 pool at the flagellar base. **(e)** An analogy for KAP loading on IFT trains. Boats (IFT trains) are
788 laden with rowers (dynein-2) with oars (kinesin-2) as they row to the right shore. At the beach,
789 the rowers get out, leave their oars on the water, and walk the boats back to the dock. Oars can
790 only be collected when they randomly float back to the left shore. If the distance between the
791 shores is large, oars build up on the water and are not readily available for new boats.
792

Supplementary Information

1. Figure Supplements

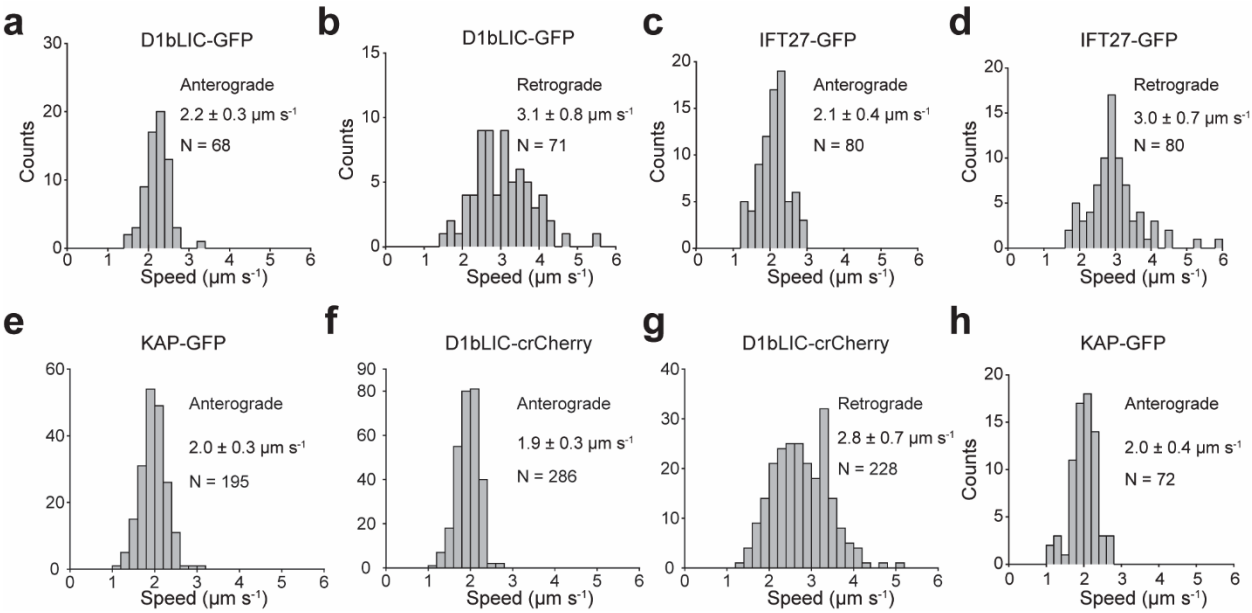

Figure 1-Figure Supplement 1. Anterograde and retrograde velocities of epitope-tagged IFT27, KAP, and D1bLIC.

(**a**) Anterograde velocities of D1bLIC-GFP in *d1blic::D1bLIC-GFP* cells. (**b**) Retrograde velocities of D1bLIC-GFP in *d1blic::D1bLIC-GFP* cells. (**c, d**) Anterograde (c) and retrograde (d) velocities of IFT27-GFP in *pf18 IFT-27-GFP* cells**.** (**e**) Anterograde velocities of KAP-GFP in *d1blic::D1bLIC-crCherry KAP-GFP* cells. (**f, g**) Anterograde (f) and retrograde (g) velocities of D1bLIC-crCherry in d*1blic::D1bLIC-crCherry KAP-GFP* cells. (**h**) Anterograde velocities of KAP-GFP in *fla3::KAP-GFP* cells. All velocities are reported as mean ± s.d.

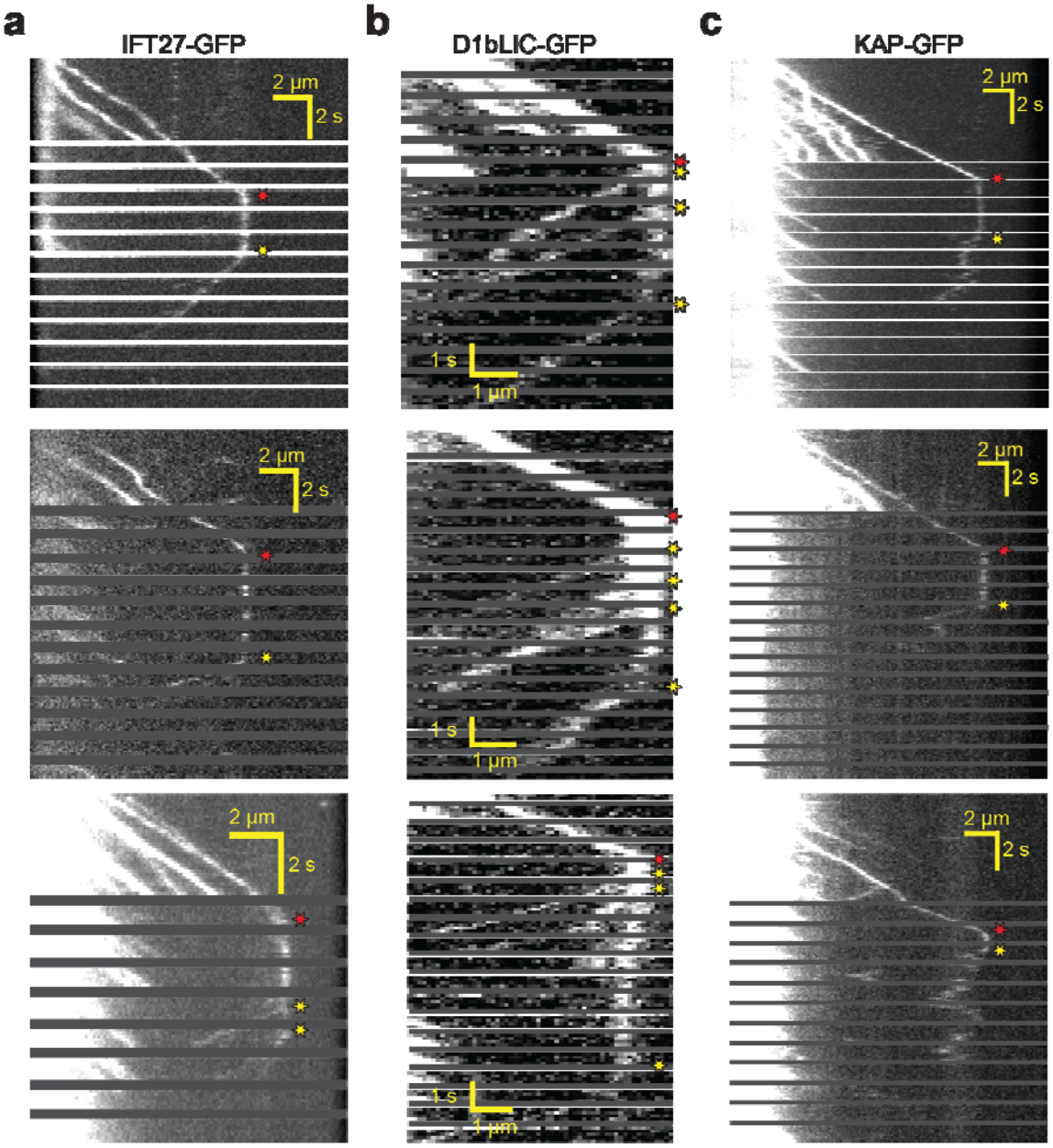

806

807 **Figure 1-Figure Supplement 2. Additional examples for PhotoGate imaging of IFT27,**

808 **D1bLIC, and KAP.**

809 (**a**) IFT27 is moved to the tip on anterograde trains, remodels, and returns to the flagellar base on

810 retrograde trains. (**b**) Dynein is moved to the tip on anterograde trains, remodels, and moves

811 retrogradely to the cell body. (**c**) Kinesin moves anterograde trains to the flagellar tip, dissociates

812 from the IFT trains at the tip, and diffuses within the flagellum. Red and yellow stars indicate

arrival to and departure from the tip, respectively.

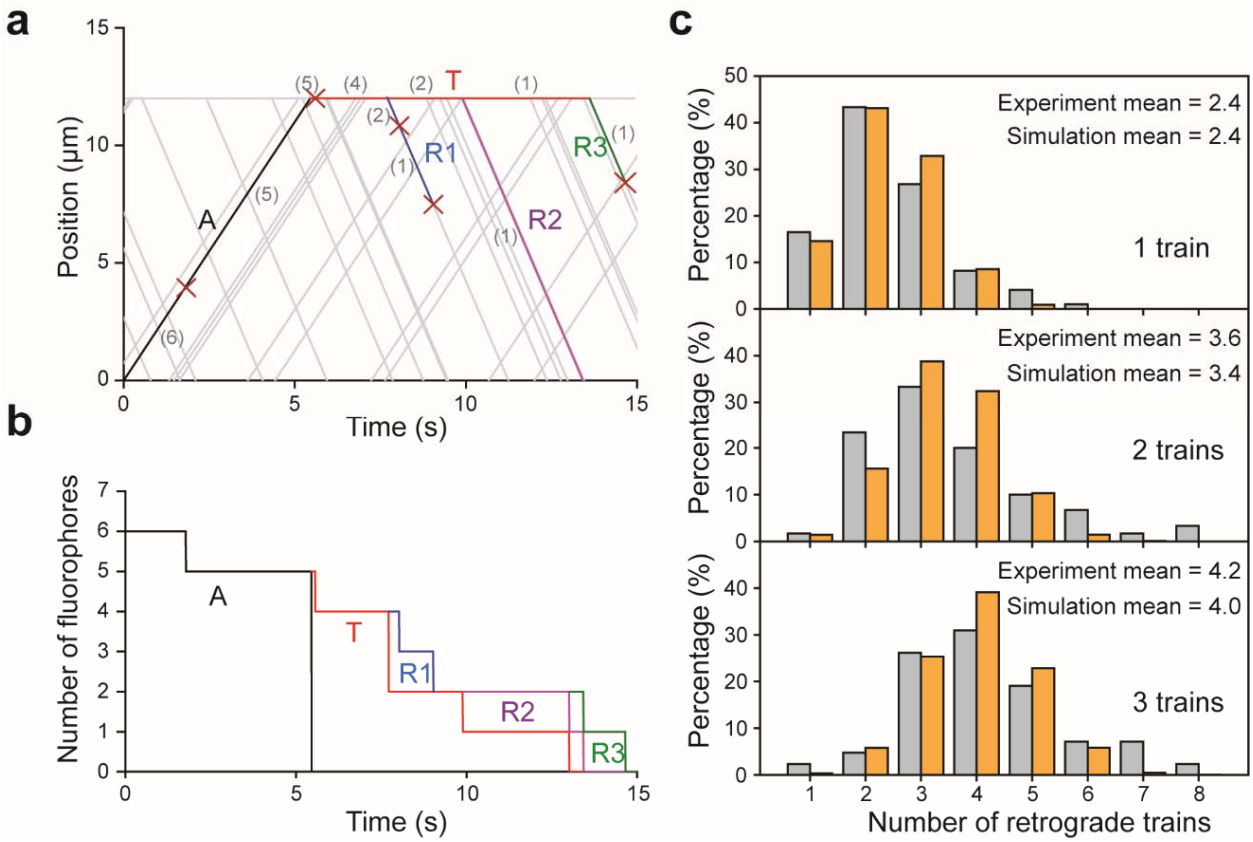

Figure 1-Figure Supplement 3. Monte Carlo simulations for the dynamics of IFT trains at the flagellar tip.

(a) A simulated kymograph with one anterograde IFT train (label A, black line) reaching the flagellar tip, joining the pool at the tip (label T, red line), and returning as three retrograde IFT trains (label R1-R3; blue, purple, and green lines). The anterograde train originally carries 6 bright fluorophores, and each fluorophore either bleaches or returns back to the flagellar base. The number of fluorophores is labeled in grey color within parentheses, and each bleaching event is indicated by a red cross. **(b)** The number of fluorophores in the anterograde train (label A, black line), at the flagellar tip (label T, red line), and the retrograde trains (label R1-R3, blue

line, purple line and green line) are shown as a function of time. Step-by-step reduction in GFP numbers in anterograde and retrograde trains is due to photobleaching of GFPs at 0.05 s^{-1} under TIR illumination. **(c)** The number of detectable retrograde trains in PhotoGate assays with one, two, and three fluorescent anterograde trains arriving at the tip. Gray and orange bars show the results of experiments in Figure 1f and Monte Carlo simulations, respectively (N = 5,000 for simulations).

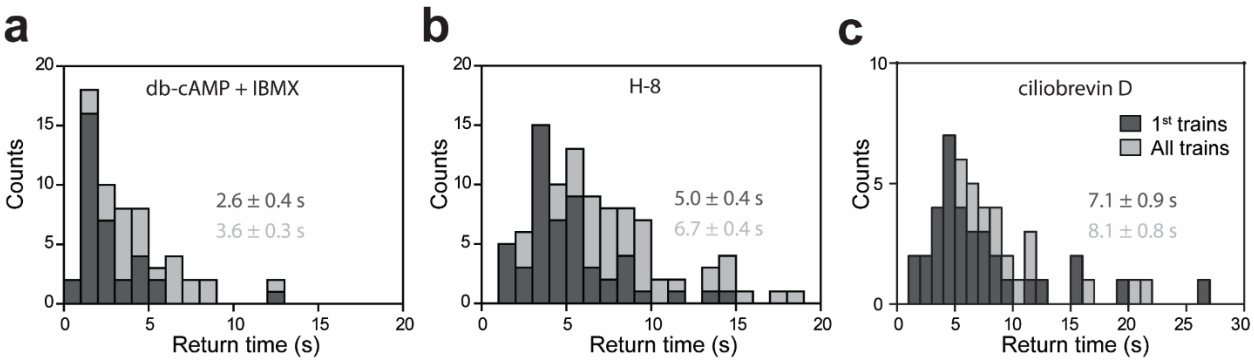

Figure 2-Figure Supplement 1. Tip return time of IFT27-GFP under various drug treatments.

(**a**) Return time histogram of IFT27-GFP with db-cAMP and IBMX treatment. N = 34 trains in 25 cells. (**b**) Return time histogram of IFT27-GFP with H-8 treatment. N = 52 trains in 32 cells. (**c**) Return time histogram of IFT27-GFP with ciliobrevin D treatment. N = 34 trains in 27 cells (mean ± s.e.m.).

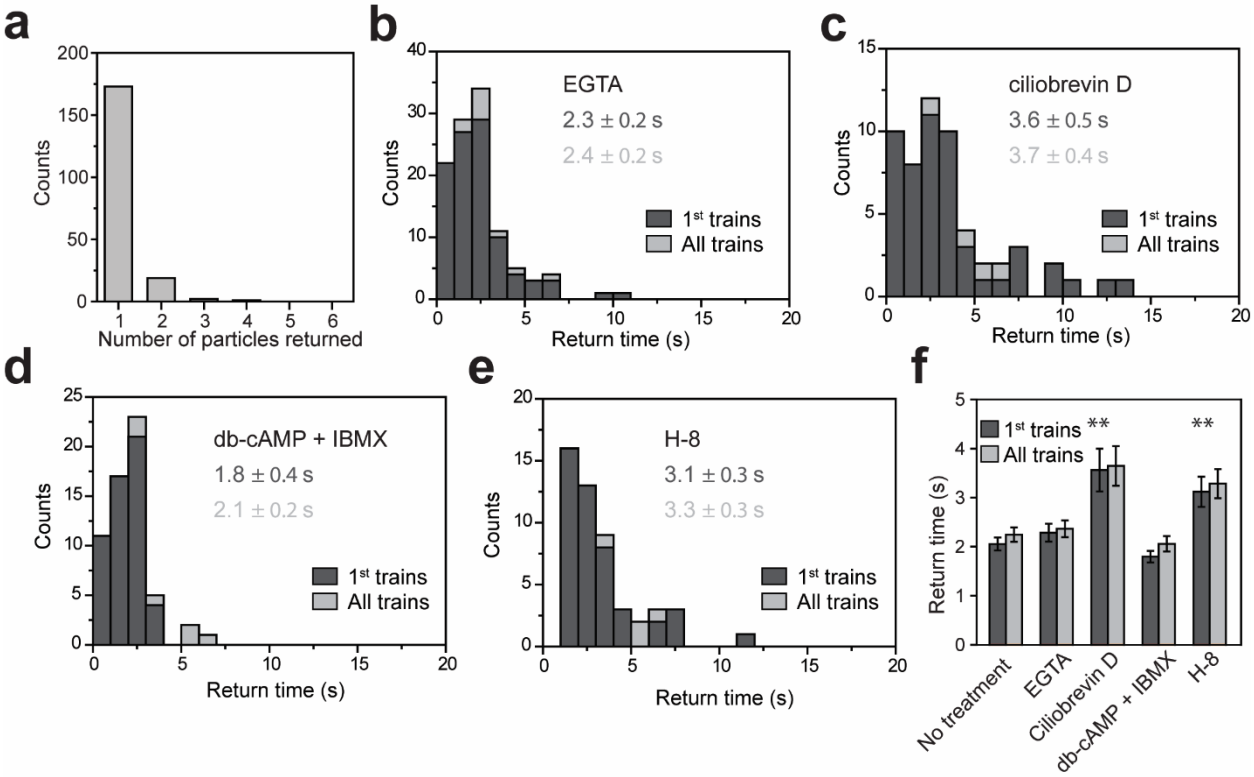

Figure 3-Figure Supplement 1. Tip return time of KAP-GFP under various drug treatments. (a) The number of fluorescent KAP particles emanating from a single fluorescent anterograde KAP particle at the tip. N = 195 trains in 106 cells over 9 independent experiments. All KAP clusters displayed diffusive movement after leaving the tip. (**b**) Return time histogram of KAP-GFP with EGTA treatment. N = 100 trains in 59 cells over 5 independent experiments. (**c**) Return time histogram of KAP-GFP with ciliobrevin D treatment. N = 52 trains in 37 cells over 4 independent experiments. (**d**) Return time histogram of KAP-GFP with db-cAMP and IBMX treatment. N = 53 trains in 28 cells over 2 independent experiments. (**e**) Return time histogram of KAP-GFP with H-8 treatment. N = 46 trains in 18 cells. (**f**) The average tip return times for KAP-GFP under various drug treatments (mean ± s.e.m.; **p < 0.01 as compared to no treatment).

853

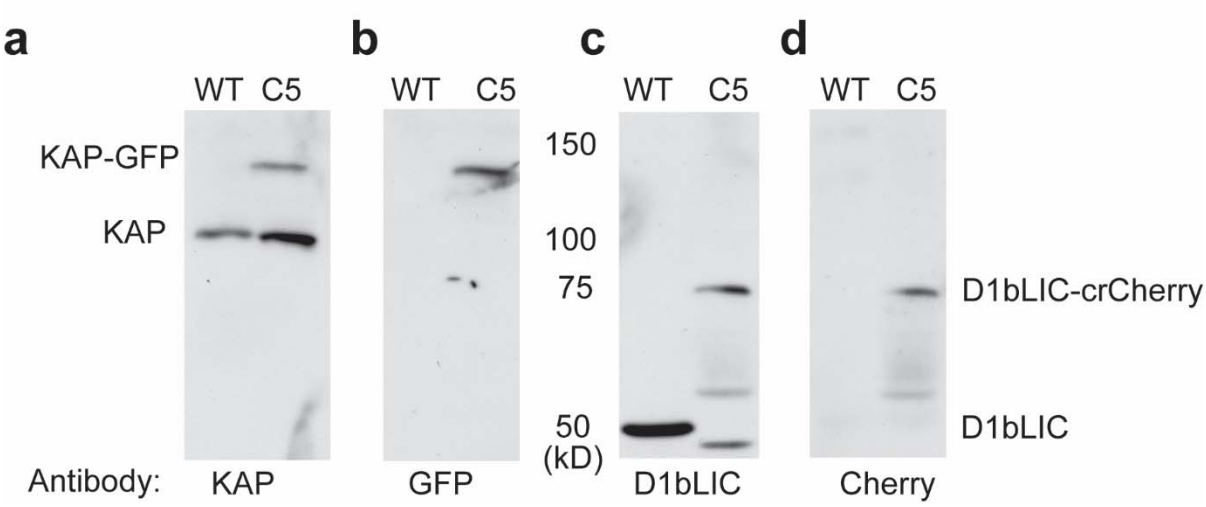

Figure 4-Figure Supplement 1. Expression of KAP-GFP and D1bLIC-crCherry in isolated flagella from a double-tagged strain.

Isolated flagella from wild-type cells (WT) and a *d1blic::D1bLIC-crCherry KAP-GFP* strain (C5) were analyzed on Western blots probed with antibodies against (**a**) KAP, (**b**) GFP, (**c**) D1bLIC, and (**d**) Cherry. The endogenous KAP subunit migrates at ~95 kD in both strains (a), and the KAP-GFP subunit migrates at ~122 kD (a, b). The D1bLIC subunit migrates at ~49 kD in WT (c) and the D1bLIC-crCherry migrates at ~75 kD in the C5 rescued strain (c, d).

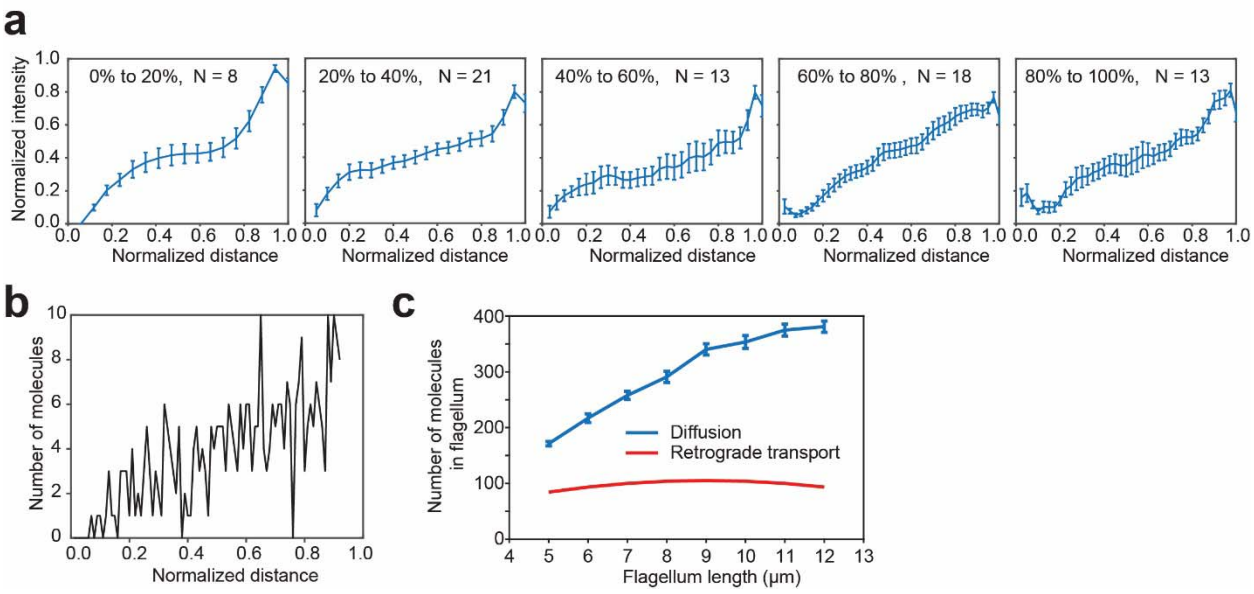

Figure 5-Figure Supplement 1. A gradient of KAP-GFP fluorescence along the length of the flagellum exists across all flagellar lengths.

(a) The gradient of KAP-GFP fluorescence is approximately linear over the length of the flagellum for flagella of different lengths. Cells undergoing flagellar regrowth were imaged and split into groups by their flagellar length. IFT trains were manually removed from kymographs and remaining pixels were time-averaged to calculate the concentration gradient of the KAP-GFP. Error bars represent s.e.m. N = 57 kymographs over 5 independent experiments. **(b)** Monte Carlo simulations reveal the flagellar distribution of KAP-GFP diffusing from a source at the tip (right) to a sink at the base (left). (**c**) Simulations show that return of KAP to the cell body by diffusion leads to a greater accumulation of KAP in the flagellum, in comparison to a hypothetical case where KAP returns to the cell body via retrograde transport. This analysis accounts for both anterogradely moving and diffusing KAP molecules.

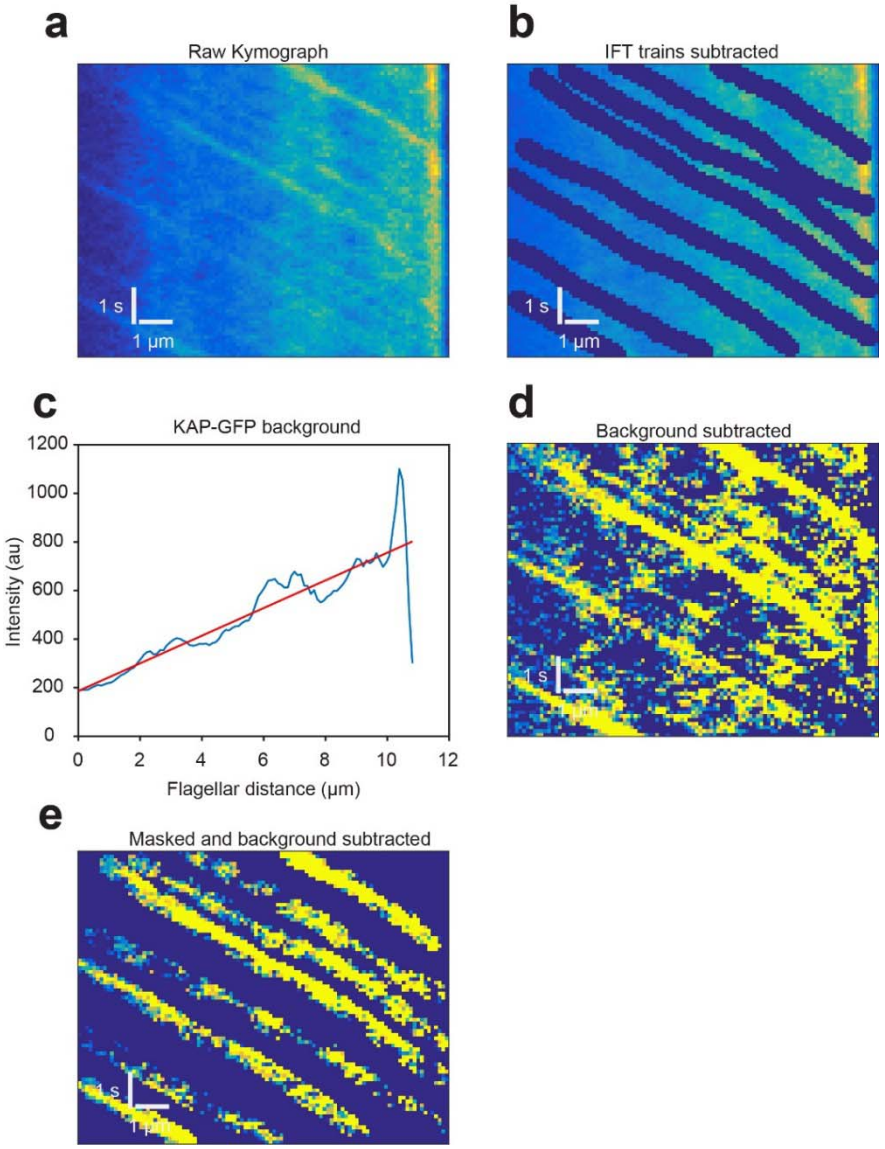

879

880 **Figure 5-Figure Supplement 2. The influx and efflux of KAP-GFP fluorescence in fully**
881 **grown flagella are equal.**

882 **(a)** An example kymograph of a *fla3::KAP-GFP* flagellum imaged with TIR. The flagellar tip is
883 on the right. **(b)** To calculate the intensity of the fluorescence background, anterograde
884 trajectories of KAP were manually subtracted from the kymograph. (**c**) Intensities were time-
885 averaged to calculate KAP-GFP background. Efflux was calculated from Fick's law using the
886 slope of the intensity profile along the flagellar length and the measured diffusion constant (1.7

887 μm^2 s^{-1}). **(d)** Background was subtracted from original kymograph to get anterograde train
888 intensities. **(e)** The kymograph was masked for anterograde trains to calculate the average
889 fluorescent counts per train. Influx was calculated by multiplying counts per train with the
890 measured train frequency (1.3 s^{-1}). KAP-GFP influx into the flagellum (1,130 ± 70 counts s^{-1})
891 was similar to the efflux of KAP from the flagellum (1,170 ± 160 counts s^{-1}). N = 57 kymographs
892 over 5 independent experiments (mean ± s.e.m.).

893

2. Video Legends

Video 1. Tracking of individual IFT trains in *Chlamydomonas*. IFT movement was visualized by TIR imaging of a surface-adhered *pf18 IFT27-GFP* cell. Green and blue arrows represent the cell body and flagellar tips, respectively. The size of the window is 15.5 × 27.6 µm. The movie was recorded at 10 frames s^{-1} and is played in real time. This video corresponds to Figure 1a.

Video 2. Observing the dynamics of single IFT trains at the flagellar tip using the PhotoGate. The distal half of the flagellum on the right of a surface-adhered *pf18 IFT27-GFP* cell is photobleached by an intense laser beam. The gate beam is turned off to allow a single anterograde train to enter the bleached region and turned on repeatedly at the base of the flagellum to bleach the subsequent anterograde trains. Two retrograde trains emanate from a single fluorescent anterograde train at the tip. Frames with the gate beam on are removed for illustration purposes. The movie was recorded at 10 frames s^{-1} and is played in real time. Cyan and magenta arrows represent anterograde and retrograde particles, respectively. Pre-bleaching frames are marked by red borders. The position of the PhotoGate is marked by a red line. This video corresponds to Figure 1c.

Video 3. Tip return dynamics of two fluorescent anterograde trains using the PhotoGate. A flagellum of a surface-adhered *pf18 IFT27-GFP* cell is photobleached. Two fluorescent anterograde IFT trains are allowed pass through the gate without photobleaching and subsequent anterograde trains were photobleached by the gate beam. After the anterograde trains reach the tip, three retrograde trains return with fluorescent signal from these trains. The movie was recorded at 10 frames s^{-1} and is played in real time. Cyan and magenta arrows represent anterograde and retrograde particles, respectively. The position of the PhotoGate is marked by a red line. This video corresponds to Figure 1d.

Video 4. Tip return dynamics of three fluorescent anterograde trains using the PhotoGate. A flagellum of a surface-adhered *pf18 IFT27-GFP* cell is photobleached. Three fluorescent anterograde IFT trains are allowed pass through the gate without photobleaching and subsequent anterograde trains were photobleached by the gate beam. The frames in which the gate beam was on were deleted for illustration purposes. After the anterograde trains reach the tip, four retrograde trains return with fluorescent signal from these trains. The movie was recorded at 10 frames s^{-1} and is played in real time. Cyan and magenta arrows represent anterograde and retrograde particles, respectively. Pre-bleaching frames are marked by red borders. The position of the PhotoGate is marked by a red line. This video corresponds to Figure 1e.

Video 5. Tip return dynamics of D1bLIC-GFP. In a surface-adhered *d1blic::D1bLIC-GFP* cell, one D1bLIC-GFP particle is allowed to pass through the gate without photobleaching and two fluorescent retrograde particles return to the base. The movie was recorded at 10 frames s^{-1} and is played in real time. Cyan and magenta arrows represent anterograde and retrograde particles, respectively. Pre-bleaching frames are marked by red borders. The position of the PhotoGate is marked by a red line. This video corresponds to Figure 3c.

Video 6. KAP-GFP dissociates from IFT trains at the tip. In the *fla3::KAP-GFP* strain, one fluorescent KAP-GFP particle is allowed to pass through the gate without photobleaching. The KAP-GFP particle undergoes diffusive motion after arriving at the flagellar tip. The size of the window is 26.6 × 16.6 µm. The movie was recorded at 10 frames s^{-1} and is played in real time. Cyan and magenta arrows represent anterograde and diffusing particles, respectively. The position of the PhotoGate is marked by a red line. This video corresponds to Figure 3f.

Video 7. Dual color imaging of KAP-GFP and D1bLIC-crCherry. The movement of KAP-GFP and D1bLIC-crCherry are simultaneously tracked in a surface-adhered *d1blic::D1bLIC-*

940 *crCherry KAP-GFP* cell. KAP and D1bLIC co-localize in the anterograde direction. D1bLIC
941 displays retrograde tracks while retrograde transport of KAP is rarely seen. KAP-GFP channel is
942 on the left and D1bLIC-crCherry channel is on the right. The movie was recorded at 8.3 frames s^{-1}
943 and is played in real time. This video corresponds to Figure 4a.

944 **Video 8. Recovery of KAP-GFP after photobleaching the middle section of a flagellum.** A
945 surface-adhered *fla3::KAP-GFP* is imaged under TIRF illumination. The middle part of the
946 flagellum is bleached by a 25 kW cm^{-2} laser beam for 0.1 s and the cell is imaged under 100 W
947 cm^{-2} TIRF excitation. The fluorescent signal recovers with different kinetics from each side of
948 the flagellum. The data was collected at 10 frames s^{-1} and is played in real time. Green and blue
949 arrows represent the cell body and flagellar tips, respectively. The photobleached area is marked
950 by thin red lines. This video corresponds to Figure 5a.

951

952